Geologic History and Crater Morphology of Asteroid (162173) Ryugu

Crater morphology and chronology of asteroid Ryugu

Y. Cho[1], T. Morota[1], M. Kanamaru[2], N. Takaki[1], K. Yumoto[1], C. M. Ernst[3], M. Hirabayashi[4], O. S. Barnouin[3], E. Tatsumi[1, 5], K. A. Otto[6], N. Schmitz[6], R. J. Wagner[6], R. Jaumann[6, 7], H. Miyamoto[1], H. Kikuchi[1], R. Hemmi[1], R. Honda[8], S. Kameda[9], Y. Yokota[8, 10], T. Kouyama[11], H. Suzuki[12], M. Yamada[13], N. Sakatani[9], C. Honda[14], M. Hayakawa[10], K. Yoshioka[1], M. Matsuoka[10], T. Michikami[15], N. Hirata[14], H. Sawada[10], K. Ogawa[16], and S. Sugita[1].

[1]The University of Tokyo, 7-3-1 Hongo, Bunkyo, Tokyo 1130033, Japan

[2]Osaka University, 1-1 Machikaneyama, Toyonaka, Osaka 560-0043, Japan

[3]The Johns Hopkins University Applied Physics Laboratory, Laurel, MD 20723, United States

[4]Department of Aerospace Engineering, Auburn University, 211 Davis Hall, Auburn, AL 36849-5338, United States

[5]Instituto de Astrofísica de Canarias, C/Vía Láctea s/n, 38205 La Laguna, Tenerife, España

[6]German Aerospace Center (DLR), Institute of Planetary Research, Rutherfordstrasse 2 12489 Berlin, Germany

[7]Free University Berlin, Institute of Geological Sciences, Malteserstrasse 74-100, 12249 Berlin, Germany

[8]Department of Science and Technology, Kochi University, 2-5-1 Akebono-cho, Kochi 780-8520, Japan

[9]Department of Physics, Rikkyo University, 3-34-1 Nishi-Ikebukuro, Toshima Tokyo 171-8501, Japan

[10]Institute of Space and Astronautical Science (ISAS), Japan Aerospace Exploration Agency (JAXA), 3-3-1 Yoshinodai, Sagamihara 252-5210, Japan

[11]Artificial Intelligence Research Center, National Institute of Advanced Industrial Science and Technology, 2-3-26, Aomi, Koto-ku, Tokyo 135-0064, Japan,

[12] Department of Physics, Meiji University, Kawasaki, 1-1-1 Higashimita, Tama-ku, Kawasaki 214-8571, Japan,

[13] Planetary Exploration Research Center, Chiba Institute of Technology, 2-17-1 Tsudanuma, Narashino 275-0016, Japan

[14] Graduate School of Computer Science and Engineering, University of Aizu, Tsuruga, Ikkimachi, Aizu Wakamatsu, Fukushima 965-8580, Japan

[15]Faculty of Engineering, Kindai University, Hiroshima Campus, 1 Takaya Umenobe, Higashi-Hiroshima, Hiroshima 739-2116, Japan

[16]JAXA Space Exploration Center, Japan Aerospace Exploration Agency, 3-3-1 Yoshinodai, Sagamihara 252-5210, Japan

Corresponding author: Yuichiro Cho (cho@eps.s.u-tokyo.ac.jp)

Key Points:

- Craters on asteroid Ryugu are documented and counted based on the high-resolution images obtained with Hayabusa2's telescopic camera.
- Crater morphology on Ryugu ranges from distinct >100-m circular depressions to <10 m smooth texture outlined by boulders.
- Crater chronology reveals multiple resurfacing events on each hemisphere 2-11 Myr ago and Ryugu's departure from the main belt < 7 Myr ago.

Abstract

Crater morphology and surface age of asteroid (162173) Ryugu are characterized using the high-resolution images obtained by the Hayabusa2 spacecraft. Our observations reveal that the abundant boulders on and under the surface of the rubble-pile asteroid affect crater morphology. Most of the craters on Ryugu exhibit well-defined circular depressions, unlike those observed on asteroid Itokawa. The craters are typically outlined by boulders remaining on the rim. Large craters (diameter >100 m) host abundant and sometimes unproportionally large boulders on their floors. Small craters (<20 m) are characterized by smooth circular floors distinguishable from the boulder-rich exterior. Such small craters tend to have dark centers of unclear origin. The correlation between crater size and boulder number density suggests that some processes sort the size of boulders in the shallow (<30 m) subsurface. Furthermore, the crater size-frequency distributions (CSFDs) of different regions on Ryugu record multiple geologic events, revealing the diverse geologic history on this 1-km asteroid. Our crater counting analyses indicate that the equatorial ridge is the oldest structure of Ryugu and was formed 23-29 Myr ago. Then, Ryugu was partially resurfaced, possibly by the impact that formed the Urashima crater 5-12 Myr ago. Subsequently, a large-scale resurfacing event formed the western bulge and the fossae 2-9 Myr ago. Following this process, the spin of Ryugu slowed down plausibly due to the YORP effect. The transition of isochrons in a CSFD suggests that Ryugu was decoupled from the main belt and transferred to a near-Earth orbit 0.2-7 Myr ago.

Plain language summary

Japan's asteroid explorer Hayabusa2 visited the carbon-rich, 1-km asteroid named Ryugu. One of the onboard cameras took many pictures of asteroid's surface. In order to know the history of this asteroid, we estimate the age of different geologic units by counting craters. We also documented how the craters on this asteroid look, to help understand the geology of the carbon-rich world. We found that the mountain range running along the equator formed some 30 million years ago. About 5-12 million years ago, the meteorite impact that formed the biggest crater on this asteroid likely scattered soil around, erasing nearby craters that existed before. Then, about 2-9 million years ago, the western half of this asteroid was wiped out by a large-scale movement of rocks and pebbles that build this asteroid, because the asteroid was spinning fast and unstable at that time. Then, sometime between 0.2 and 7 million years ago, this asteroid left the home of asteroids located between Mars- and Jupiter orbits, and came to the orbit passing near the Earth. During its journey to the near-Earth orbit, the spin of the asteroid slowed down because of the very weak but effective force by heat radiation from surface rocks.

1 Introduction

(162173) Ryugu is a top-shaped C-type asteroid explored by the Hayabusa2 spacecraft. A series of observations by the telescopic optical navigation camera (ONC-T) and the near infrared spectrometer (NIRS3) revealed the geomorphology and visible/near infrared spectra of this asteroid (Sugita et al., 2019; Kitazato et al., 2019). Ryugu exhibits an equatorial ridge and an east-west dichotomy outlined by two fossae (Sugita et al., 2019; Watanabe et al., 2019). The western hemisphere, which exhibits the western bulge that stretches approximately 180-300°E, is characterized by slightly (a few %) darker v-band albedo (Sugita et al., 2019) and a smaller number density of boulders (Michikami et al., 2019) compared with the eastern hemisphere. The different characteristics between the two hemispheres suggest different lithologies and/or a complex geologic history on this small, 1-km-diameter asteroid. The equatorial ridge shows spectral slopes bluer than mid-latitudinal regions, suggestive of mass movement away from the equator or lithology/surface properties different from the rest of the asteroid (Sugita et al., 2019, Morota et al., 2020). The coincidence of the east-west dichotomy with the fossae suggests that global deformation played a key role in forming the dichotomy (Kikuchi et al., 2019; Hirabayashi et al., 2019). However, the mechanism responsible for the east-west dichotomy formation remains unclear. The homogeneous surface normal albedo (Yokota et al. in revision) of the whole surface does not support a simple two-body merge scenario as the origin of the dichotomy. Proposed hypotheses include structural deformation under fast rotation in the past (Hirabayashi et al., 2019) and consequences of large oblique impact on Ryugu (Matsumoto et al., 2020). Thus, determining the ages of both hemispheres is key to understand the evolution of Ryugu.

As with other asteroids that have been explored by spacecraft, impact craters are among the most ubiquitous geologic features on Ryugu. Investigating the crater statistics and morphology gives hints on the geologic history of the asteroid, crater erasure processes, spin evolution, subsurface structures that are otherwise hidden, and physical properties of the surface. For example, the initial report by Sugita et al. (2019) showed that the crater model age of Ryugu ranges from 9 Ma to 160 Ma depending on the degree of cohesion of the surface materials. Their study, however, was based on a global crater counting analysis, which did not take the different geologic units into account and therefore could simplify the complex history of Ryugu. For example, the east-west dichotomy and the bluer color of the equatorial ridge suggest different geologic histories, surface properties, or ongoing mass movement on these units. Subsequently, more detailed investigation on the spatial distribution of craters was

conducted, finding a latitudinal variation in crater number density (Hirata et al., 2020). Crater depth-to-diameter (d/D) ratios were then measured based on the shape model of Ryugu (Noguchi et al., 2021).

However, the ages of individual geologic events have not been studied. Detailed morphology of craters on Ryugu, which is important for chronologic and geologic investigation, has not been studied extensively yet either. Understanding crater populations at the smaller size range (diameter < 20 m) is also important for providing insights into more recent, or potentially ongoing geologic processes on Ryugu. Smaller craters can be statistically considered to have formed more recently than much larger ones. Therefore, the size-frequency distributions of such small craters may constrain the timescale of their formation and erasure processes, which directly control the surface geology of the asteroid. The global crater size-frequency distribution (CSFD) measured by Sugita et al. (2019) showed the paucity of small craters (20-30 m) on Ryugu, suggesting that the smaller craters are likely erased by some surface processes, such as ejecta blanketing, seismic shaking, or regolith convection (Miyamoto et al., 2007). Morphological observation is useful for examining such size-sorting processes. In fact, the SCI impact experiment showed that a large amount of ejected materials came back to the surface, leading to material burial in a relatively wider regions (Arakawa et al., 2020). Better understandings of the small crater statistics would also shed light on the unique orbital evolution that Ryugu may have experienced recently (Morota et al., 2020).

Surface age can give constraints on the spin evolution of Ryugu as well. Recent work using finite element analyses implies that Ryugu's top shape was made by global deformation under a fast spin state (~3.5 hr period) in the past (Hirabayashi et al., 2019; Watanabe et al., 2019). The fast-spin state might have been achieved upon the gravitational reaccumulation of Ryugu after the catastrophic disruption of the parent body that made this rubble-pile asteroid (Michel et al., 2020). Later, Ryugu's spin may have stochastically evolved (Statler, 2009; Bottke et al., 2015) but eventually slowed down to the current spin period of 7.6 hr by the Yarkovsky-O'Keefe-Radzievskii-Paddack (YORP) effect. The duration of the fast spin state and the timescale of spin-state evolution are key observables to test this YORP-induced spin-evolution hypothesis.

The morphology of impact craters is also important information to understand the cratering processes in a microgravity environment and surface/subsurface properties of a rubble pile asteroid, including porosity (Wünnemann et al., 2006), boulder-surface interaction (Tatsumi & Sugita, 2018), and subsurface structure (Hirata et al., 2009 for Itokawa; Veverka

et al., 1999 for Mathilde; Bart et al., 2011). Steep local topography usually seen on craters allows investigation of the surface modification process and the surface properties. Craters may also be used to see vertical structure, such as subsurface layers with distinct strength (Arakawa et al., 2020).

The purpose of this study is to determine the ages of major geologic events by means of crater chronology and morphological investigation of craters. In this study, we use high-resolution images of Ryugu that have been obtained since the initial global observations (Kitazato et al., 2019; Sugita et al., 2019; Watanabe et al., 2019) to further characterize the statistics and morphology of craters. We identify crater candidates within these images and build a new catalogue of craters down to 3 m in diameter. Then, we estimate both relative and absolute ages of individual geologic units based on crater chronology (section 4). Finally, using the newly established crater list and CSFD, we will discuss the geologic history of this C-type asteroid from the catastrophic disruption of its parent body through its transfer to the current near-Earth orbit. The spin-state evolution is also discussed based on the surface ages.

2 Data and Methods

The dataset, crater morphological levels, definition of geologic units, and method used to derive crater statistics are described in this section.

2.1 Dataset

We used ONC-T v-band (i.e., 550 nm) images obtained from multiple altitudes, including global image data from 20 km (i.e., Hayabusa2 spacecraft's nominal hovering altitude) and 5 km (mid-altitude operation), as well as those of limited coverage from 3 km. The spatial resolutions of these images were approximately 2, 0.5 and 0.3 meters per pixel (m/pix), respectively. Craters were visually identified with the image data globally acquired from the altitude of 5 km while Ryugu spins 360° (global observation campaign). Multiple stereo image pairs covering Ryugu were also produced from these images and used for finding circular depressions, taking the spatial distribution of boulders and surface textures into account. Then individual images were mapped on the shape model of Ryugu (SHAPE_SFM_3M_v20180804; Watanabe et al., 2019) to derive the diameter and location of each candidate crater (circular feature). The *small body mapping tool* (sbmt) was used for this analysis. Each candidate crater was categorized into different confidence levels based on individual morphology (Section 2.2). We also used even higher-resolution images (0.2 m/pix) obtained during the low-altitude operation dedicated to find the crater formed by the Small

Carry-on Impactor (SCI) in April 2019 (Arakawa et al., 2020), to identify and measure craters smaller than 20 m. This SCI crater-search mosaic covers an area of 0.37 km^2 (~14% of the entire surface) at approximately 50°N-50°S and 260-340°E, which spans both eastern hemisphere and western bulge. Craters smaller than 10 pixels (2 m for those imaged during the SCI crater-search campaign) were regarded at the resolution limit. The phase angles of the images used for the global observation and SCI crater search were 15°-32° and 20°-27°, respectively. All images were processed using the standard calibration pipeline (Suzuki et al., 2018; Tatsumi et al., 2019). Crater color indices, such the ratio of *b*-band (0.48 μm) and *x*-band (0.86 μm) reflectance (*b*/*x* slope) and a color contrast between crater interior and exterior ("red/blue" identifier), were measured by Morota et al. (2020) and cited in this study. The depth-to-diameter ratios (*d*/*D*) of individual craters (Noguchi et al. 2021) were cited in our crater catalogue as well.

2.2 Crater morphological levels

We investigated every stereo pair and found that crater candidates have different degrees of morphological confidence from clear circular depressions to rather ambiguous quasi-circular features without obvious depressions. The confidence levels of craters found in this study were assigned based upon the following definitions. Confidence level 1 (CL1) is a circular depression with a crisp circular rim; CL2 is a depression with a more ambiguous but circular rim; CL3 is a quasi-circular depression with a partially circular rim suggestive of perturbed or broken crater rim; CL4 is a quasi-circular feature defined by a circular pattern of boulders. The CL4 crater candidates exhibit no resolvable and quantifiable depression in their interior. Note that the confidence levels can be affected by viewing geometry and illumination effects, so CLs 1 and 2 may occasionally be interchangeable. Future studies focusing on crater profile measurements may revise the CLs derived in this study, but our classification is sufficient for the scope of this survey. We regarded the candidates of CL1-3 as impact craters and used them for the following crater size-frequency distribution (CSFD) analyses. It was difficult to establish the threshold of the crater depth between CL 3 and CL 4 because of multiple factors, such as presence of boulders on crater floors, lighting condition, viewing geometry, and uncertainty of the shape model. Nevertheless, the overall distribution of *d*/*D* ratios of the craters on Ryugu (Noguchi et al., 2021) suggest that the craters shallower than $d/D = 0.05$ are not detected as a depression.

212 2.3 Geologic units

213 In this study, we categorized the surface of Ryugu into multiple units: the eastern
214 hemisphere (EH), western bulge (WB), equatorial ridge (EQR; Ryujin Dorsum), high latitudes,
215 and trough (Figure 1). The eastern and western hemispheres, which show different boulder
216 number densities and v-band albedo at the phase angle of 30˚, are divided by the Horai and
217 Tokoyo Fossae, the narrow depression systems possibly connected to each other around the
218 south pole (Sugita et al., 2019). The areas of eastern and western hemispheres are 1.77 and
219 0.93 km^2 including the ridge, respectively. The high-resolution crater observations
220 compensate for such small counting area by allowing us to find > 100 craters down to a few
221 m in diameter (Section 3), while the small number statistics still potentially obscures subtle
222 differences in absolute ages. The western bulge is defined as a hemispherical region outlined
223 by the fossae, reaching the equatorial ridge at 180°E and 300°E. The eastern hemisphere is
224 defined as the remainder of the asteroid's surface. In this study, the equatorial ridge was
225 defined by the belt centered at the equator with a width of ~160 m (10°N to 10°S), which
226 corresponds to elevation higher than ~30 m (Kikuchi et al., 2020). The ridge coincides with
227 the area characterized by bluer spectral slopes (Sugita et al., 2019). The equatorial belt (0.58
228 km^2) spans both the eastern hemisphere and western bulge. The regions with the latitudes
229 higher than 10°N or 10°S were also defined to compare the crater population at the equator
230 and that at higher latitudes. The total area of the two fossae, defined by Sugita et al. (2019),
231 is 0.18 km^2. Individual craters are assigned to the units based on the location of their centers.
232 Because the equatorial ridge spans both hemispheres, craters on the ridge were also assigned
233 to either EH or WB. For example, a crater at the ridge on the eastern hemisphere is categorized
234 into both EH and EQR in the CSFDs.

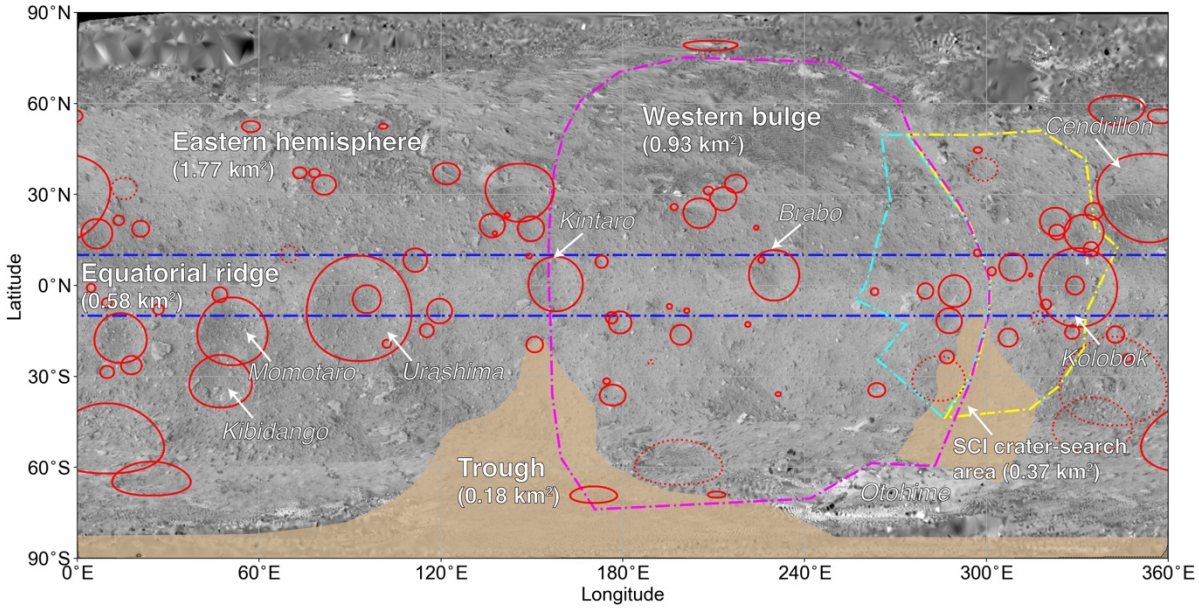

Figure 1. Definition of the crater-counting areas overlaid on a global map (dark blue: equatorial ridge, magenta: western bulge, yellow and sky-blue: SCI crater search footprints on the eastern hemisphere and western bulge, respectively). Fossae are highlighted in brown. The eastern hemisphere is defined by the entire area outside the western bulge. Craters found by the global survey in this study are shown as well (red circles; solid circles are those with confidence levels (CLs) 1-3, dotted circles are those of CL 4).

2.4 Crater size-frequency distributions (CSFDs)

The cumulative CSFDs were constructed for the individual units and fitted with crater chronology model functions. No binning was used for the plots. Resulting absolute model ages depend on model assumptions, such as crater production function, chronology function, and crater scaling rules. The surface properties, including target density, porosity, cohesion, and boulder size, were incorporated into the crater scaling rule as input parameters. We adopted the models and parameters employed by Sugita et al. (2019) and Morota et al. (2020) in deriving absolute model ages (Table 1). The models used the intrinsic collision probabilities P_i for both main-belt asteroids (MBA) and near-Earth asteroids (NEA), the population of MBAs and NEAs (Bottke et al., 2005; O'Brien and Greenberg 2005), and mean impact velocities in each orbit (Bottke et al., 1993, 1994). The two models were used to examine the model dependence of ages, as well as to derive residence time in each orbit. Error bars associated with each data point were calculated by $\pm N^{1/2}/S$, where N is the cumulative number of craters and S is the area of individual units. Errors in model ages reflect uncertainties in counting statistics and do not

include any systematic uncertainties in the crater chronology functions. The crater scaling rule by Tatsumi & Sugita (2018) was used to address the armoring effect on the boulder-rich surface of Ryugu. We assumed that the cohesion of Ryugu is neglectable and the gravity controls the crater formation (i.e., gravity scaling) to calculate the absolute age of each geologic unit (Arakawa et al., 2020). We also assumed that these surface conditions hold for the entire Ryugu surface. The sources of the model uncertainty include the target disruption energy Q_D* and impactor population. For example, changing Q_D* from 1000 J/kg to 100 J/kg would yield a factor of three younger model age. This uncertainty will be addressed when the disruption energy of Ryugu's material is determined with the returned samples. Furthermore, the impactor size-frequency model from Bottke et al. (2005) to O'Brien & Greenberg (2005) would yield a ~30% younger model age because the number of small impactors is greater in the latter model.

The software tool *craterstats* was used to fit the observed CSFDs to the crater production function and to derive fitting errors (section 4). The crater diameter ranges and number of craters used for the fitting were 70-80 m (6 craters) and > 100 m (11 craters) for the global crater data; 10-15 m for the SCI crater-search area (10 craters); > 100 m for the equatorial ridge (4 craters); 60-100 m (11 craters) and > 120 m (8 craters) for the eastern hemisphere; > 50 m (8 craters) for the western bulge; > 40 m for the north (15 craters) and south (14 craters) hemispheres. In addition to the cumulative plots, R-plots were also constructed to observe differential size-frequency distributions of the craters. Three diameter data were binned to improve the statistics. They were also used to estimate the crater retention ages at different crater diameters by the intersections between the CSFDs and multiple isochrons (Section 4.4).

Table 1. *Parameters for Crater Chronology Models Used in this Study.*

Parameters	Values	References
Intrinsic collision probability (10^{-18} /km^2/yr)	2.86 (MBA), 15.3 (NEA)	Bottke et al. (2005), O'Brien & Greenberg (2005)
Impact velocity (km/s)	5.3 (MBA), 18.0 (NEA)	Bottke et al. (1993, 1994)
Surface gravity (m/s^2)	0.00015	Watanabe et al. (2019)
Target density (kg/m^3)	1190	Watanabe et al. (2019)
Impactor density (kg/m^3)	2300	
"Dry soil" conditions		Tatsumi & Sugita (2018)

μ_1	0.41	
K_1	0.24	
μ_2	1.23	
K_2	0.01	
Effective strength (MPa)	0	
Target grain size (m)	3	Sugita et al. (2019)
Target disruption energy (J/kg)	1000	Flynn & Durda (2004)

3 Crater morphological observation

In this section, the morphology of craters on Ryugu is documented. In section 3.1, by taking advantage of the high-resolution images obtained during several descent operations, we conduct crater characterization and update the list of crater candidates published previously (Sugita et al., 2019; Hirata et al., 2020). In section 3.2, we describe the details of selected craters on Ryugu. In section 3.3, we discuss the morphological features of craters in different size ranges. In section 3.4, we discuss the possible subsurface structure of Ryugu.

3.1 Crater candidates and their morphology

More than 100 crater candidates larger than 10 m were found on Ryugu as a result of the present crater survey (Table 2). We newly identified 40 crater candidates, including 15 candidates larger than 10 m (crater IDs 87-101). Crater candidates larger than 3 m were also identified and used to construct size-frequency distributions. Ten crater candidates are larger than 100 m in diameter; 36 candidates are larger than 50 m. Despite the boulder-rich surface, craters on Ryugu are more easily identifiable than those on the rubble-pile asteroid Itokawa (Hirata et al., 2009). Ryugu's larger size and comparatively homogeneous topography could be responsible for this difference.

Table 2. *List of Candidate Craters on Ryugu and their Characteristics.*

ID	Name	Lat.	Lon.	Diameter	Confidence Level	Spectral slope [μm^{-1}]		Depth-to-diameter ratio *d*/*D*	Geologic Unit
		[degree]	[degree]	[m]		*b*/*x* slope	Color contrast		
1	Urashima	-7.2	93.0	290.1	1	0.144	red	0.07	EQR, EH
2	Cendrillon	28.3	353.7	224.0	2	0.157	red	0.11	EH
3	Kolobok	-0.7	330.3	220.7	2	0.134	red	0.08	EQR, EH
4	Momotaro	-14.8	51.2	182.5	1	0.131	red	0.12	EH
5		-50.6	9.8	173.1	3	0.150	red	0.07	EH

6	Kintaro	0.4	157.8	154.3	2	0.123	red	0.07	EQR
7		30.4	146.0	145.1	2	0.152	red	0.07	EH
8	Brabo	3.2	230.0	142.3	1	0.120	red	0.06	EQR, WB
9		-17.2	14.3	132.7	2	0.133	blue	0.12	EH
10	Kibidango	-31.5	47.3	131.2	1	0.130	blue	0.13	EH
11		17.0	332.2	99.8	1	0.130	red	0.10	EH
12		-1.9	289.5	90.2	2	0.122	red	0.08	EQR, WB
13		-63.7	24.5	85.0	3	n/a		0.09	EH
14		16.9	6.4	79.0	3	0.189	red	0.09	EH
15		-4.5	95.5	78.9	3	n/a		0.15	EQR, EH
16		6.0	308.7	77.1	1	0.095	red	0.07	EQR, EH
17		23.7	205.3	76.2	2	0.122	red	0.10	WB
18		20.9	322.7	73.9	2	0.125	red	0.09	EH
19		57.7	343.0	73.3	2	n/a		0.10	EH
20		-11.6	287.7	69.0	3	0.150	red	0.06	WB
21		-8.4	119.5	69.0	1	0.068	blue	0.08	EQR, EH
22		8.3	111.5	65.8	3	0.122	red	0.08	EQR, EH
23		18.6	149.7	65.8	2	0.129	red	0.07	EH
24		19.7	136.9	62.1	2	0.140	red	0.12	EH
25		-12.2	179.1	61.0	2	0.123	red	0.09	WB
26		28.5	213.2	58.2	2	0.124	red	0.08	WB
27		-16.3	199.1	53.6	2	0.139	red	0.07	WB
28		36.8	121.8	52.2	3	n/a		0.08	EH
29		-36.2	176.7	51.3	3	0.159	red	0.08	WB
30		-0.1	329.2	51.3	2	0.139	red	0.12	EQR, EH
31		-17.2	307.2	48.8	2	0.080	blue	0.07	EH
32		33.1	81.4	48.4	3	0.163	red	0.09	EH
33		-26.3	17.8	46.6	2	0.125	red	0.11	EH
34		-1.9	279.9	44.2	2	0.072	blue	0.06	EQR, WB
35		33.5	217.3	44.1	3	0.092	red	0.06	WB
36		24.4	335.5	43.1	3	0.158	red	0.10	EH
37		-3.1	47.0	42.7	1	0.153	red	0.10	EQR, EH
38		18.6	20.9	42.5	3	0.157	red	0.10	EH
39		-69.0	170.4	41.7	3	n/a		0.12	EH, TR
40		-19.5	150.9	41.4	3	0.126	red	0.08	EH, TR
41		11.9	334.5	39.9	1	0.057	blue	0.13	EH
42		17.5	323.3	39.7	2	0.101	blue	0.08	EH
43		-15.4	328.3	37.2	2	0.053	blue	0.13	EH
44		-14.9	115.3	36.5	2	0.112	red	0.09	EH
45		55.8	357.5	36.0	2	n/a		0.11	EH
46		7.8	173.0	34.6	1	0.078	blue	0.10	EQR, WB
47		-34.5	263.8	34.4	1	0.090	blue	0.11	WB
48		-10.7	176.3	32.0	2	0.143	red	0.10	WB
49		-28.6	9.8	30.6	3	0.122	red	0.06	EH
50		-7.9	26.8	29.3	3	0.071	blue	0.06	EQR, EH
51		-6.3	319.7	28.1	3	0.103	red	0.08	EQR, EH
52		-5.8	9.8	27.6	3	0.088	blue	0.06	EQR, EH
53		52.4	57.3	27.5	2	n/a		0.11	EH
54		37.1	73.4	26.5	3	0.082	blue	0.09	EH
55		79.0	209.0	26.0	2	n/a		0.11	EH
56		21.4	13.7	25.3	3	0.136	blue	0.11	EH
57		-0.9	4.5	24.4	3	0.060	blue	0.05	EQR, EH
58		4.6	301.7	23.6	1	0.101	red	0.07	EQR, EH
59		-24.0	346.6	21.7	3	n/a		0.08	EH
60		-19.3	102.1	21.5	3	0.158	red	0.11	EH
61		-2.1	263.1	21.0	2	0.067	blue	0.07	EQR, WB
62		37.0	78.2	20.9	3	0.150	red	0.09	EH
63		31.2	208.3	20.2	3	0.057	blue	0.12	WB

64	8.4	225.7	17.2	1	0.138	red	0.07	EQR, WB
65	25.8	197.0	16.2	2	0.109	blue	0.08	WB
66	-69.0	211.0	16.0	2	n/a		0.04	EH, TR
67	-31.6	174.7	14.5	2	0.118	blue	0.07	WB
68	-7.0	195.4	14.4	3	0.123	blue	0.05	EQR, WB
69	9.6	149.1	14.0	1	0.102	blue	0.09	EQR, EH
70	-8.4	201.1	14.0	2	0.111	blue	0.07	EQR, WB
71	-12.9	221.3	13.9	2	0.112	blue	0.07	WB
72	52.4	100.9	12.6	2	n/a		0.08	EH
73	23.2	141.9	12.5	2	0.146	red	0.06	EH
74	17.2	137.8	11.4	2	n/a		0.04	EH
75	19.0	224.0	11.2	2	0.102	blue	0.08	WB
76	-35.9	231.3	10.5	2	0.102	blue	0.07	EH
77	3.4	314.6	10.0	2	0.081	blue	0.03	EQR, EH
78	-31.2	341.7	223.0	4				EH
79	-45.9	335.0	133.0	4				EH
80	-30.6	284.2	112.0	4				WB
81	-58.4	198.4	112.0	4				EH
82	38.2	298.9	55.8	4				EH
83	31.9	15.4	53.0	4				EH
84	10.3	69.9	46.7	4				EH
85	-10.6	317.0	35.0	4				EH
86	-25.4	189.2	11.4	4				WB
87	-16.2	342.6	45.0	2				EH
88	-23.6	287.0	33.3	3				WB
89	10.7	297.0	18.9	2				WB
90	44.6	297.2	14.3	3				EH
91	19.1	303.7	13.2	4				EH
92	-7.8	269.4	12.5	3				EQR, WB
93	24.4	314.3	12.3	2				EH
94	1.1	291.0	12.1	2				EQR, WB
95	14.4	279.5	11.9	3				WB
96	-22.3	290.3	11.9	2				WB
97	28.5	325.1	11.1	2				EH
98	3.5	270.1	10.8	2				EQR, WB
99	6.3	280.5	10.4	3				EQR, WB
100	35.2	308.9	10.3	4				EH
101	21.2	286.2	10.3	4				WB
102	12.0	292.3	9.8	2				WB
103	-4.4	281.8	9.0	3				EQR, WB
104	10.9	321.4	8.9	2				EH
105	13.0	292.6	8.4	2				WB
106	-4.4	304.2	8.3	2				EQR, EH
107	-3.8	259.1	7.7	3				EQR, WB
108	16.4	280.5	7.7	3				WB
109	5.2	287.3	7.3	3				EQR, WB
110	25.8	313.2	6.8	3				EH
111	8.4	283.9	6.4	2				EQR, WB
112	10.3	278.3	6.1	3				WB
113	10.4	271.1	5.7	1				WB
114	15.2	324.4	5.7	2				EH

115	45.4	272.5	5.6	2	WB
116	18.1	305.0	5.2	4	EH
117	-11.6	289.6	5.1	2	WB
118	-1.2	304.5	4.8	2	EQR, EH
119	-15.4	304.8	4.4	2	EH
120	0.6	273.5	4.3	3	EQR, WB
121	1.0	284.0	4.2	3	EQR, WB
122	3.3	272.8	4.0	2	EQR, WB
123	19.8	296.3	3.1	2	WB
124	8.6	280.9	2.9	2	EQR, WB
125	0.7	266.2	2.7	2	EQR, WB
126	4.8	212.4	9.0	2	EQR, WB

Note. 40 crater candidates have been added to the list in Hirata et al. (2020). Half of the craters smaller than 20 m were found in the high-resolution images obtained during the SCI-crater-search operation. Crater IDs are based on Hirata et al. (2020). Depth-to-diameter ratios (d/D) are from Noguchi et al. (2021). Crater color indices (b/x slope and "red/blue" identifier) are from Morota et al. (2020). Note that newly identified craters are not necessarily sorted by diameter. Geologic units: eastern hemisphere (EH), western bulge (WB), equatorial ridge (EQR), trough (TR).

3.2 Observations of prominent craters on Ryugu

Here we document individual craters exhibiting prominent features, which may have important information for Ryugu's history, geology, and impact cratering process. Included are seven craters larger than 100 m in diameter, some smaller craters around them, and a few less obvious crater candidates. We selected the large craters because CSFDs suggest that those larger than 100 m were not significantly modified by subsequent erasure processes and thus record crater formation on Ryugu more directly. Also, they are large enough for the observation of their floors, while smaller craters are more subject to degradation (discussed in Section 4). These craters exhibit a variety of morphological features and are representative of individual units: the largest crater Urashima on the equatorial ridge, Momotaro and Kibidango as a large crater doublet spanning from the ridge to a high latitude in the southern hemisphere, Cendrillon at a high latitude in the northern hemisphere, Kolobok on the most heavily cratered region, Kintaro on the rim of the trough, and Brabo on the western bulge.

Furthermore, boulders associated with the craters are described in this section because crater formation on a rubble-pile asteroid involves fragmentation, ejection, and displacement of boulders. Boulder number density, size, and shapes thus have the information on original surface/subsurface structure and/or crater formation processes. In fact, size-sorting of boulders was observed at the artificial impact experiment (Kadono et al., 2020): some boulders were excavated but left on the floor, while finer materials were ejected. This observation suggests

that some boulders on the crater floors represent material originally buried in the subsurface. Thus, observing the boulders in craters is important for characterizing Ryugu's geology in the vertical direction.

Urashima (7°S, 93°E, 290 m) is the largest crater on Ryugu (Figure 3a). The northern rim of the crater cuts the equator, excavating the original ridge by approximately 40 m in depth. Despite Urashima's deep excavation, the largest boulder found in Urashima is approximately 20 m in size on its western rim. The small number of such large boulders in this crater, as compared to the half-diameter Kibidango crater (described in the following paragraph) implies that the subsurface of the equatorial ridge is composed of relatively fine materials compared to the high-latitudes. The eastern side of the rim is lower than the western side, forming a 100-m wide plateau. The cross section of Urashima is a conical shape (Namiki et al., 2019) which is often observed in laboratory cratering experiments on granular material (e.g., Oberbeck, 1971). The conical shape might have been formed by slumping of crater walls as is seen in experiments. This observation suggests that the post-impact modification stage was controlled by the gravity even though it is very low on Ryugu. Darker materials are exposed at the bottom of this crater, the feature consistent with the morphology of the SCI crater (Arakawa et al., 2020). This dark deposit, which remains dark with a photometric correction (Sugita et al., 2019), could be due to either dark, rough, or porous material (Cloutis et al*.,* 2018). Other hypotheses include crushed dark boulder, remnant of a dark impactor, or possibly another stratigraphic layer exposed on the crater bottom. Shock darkening or impact melt is unlikely because of the low shock pressure expected on Ryugu (Keil et al., 1997). Traces of mass wasting are observed in this largest crater. A possible 80-m wide, 5-m thick slump is observed on its southeastern wall, whose leading edge makes the crater bottom appear a deep pit (Figure 2b). The slope-facing flanks of some boulders on the northwestern wall (boulders B1 and B2) are covered by finer materials, while their opposite sides are not. This feature is the evidence for smaller-scale downslope regolith migration into this crater. A slope streak (Kikuchi et al., 2019, Sugita et al., 2019) on the southwestern wall are well resolved as a boulder chain at this image resolution (Figure 2b). A very large boulder named *Ejima saxum* (~60 m wide, ~30 m tall) sits just outside the southern rim. The northwestern side of Ejima saxum exhibits a sharp flank running parallel to Urashima's rim, while the other facets exhibit hummocky surfaces with gentler slopes.

The craters named *Momotaro* (15°S, 51°E, 183 m) and *Kibidango* (31°S, 47°E, 131 m) are a relatively fresh-looking example of crater doublet (Figure 2d). These craters were most likely formed by two separate impacts, given the comparable crater sizes and low speed of

ejected material to make secondary craters. Stratigraphically, the southern crater Kibidango overlies Momotaro because the northern rim of Kibidango intrudes into the Momotaro crater. Nevertheless, the latter Kibidango-forming impact did not significantly destroy the morphology of predated Momotaro. This observation suggests a low seismic efficiency (i.e., the conversion ratio of impactor's kinetic energy to seismic energy) on Ryugu, which is consistent with the artificial impact experiment by SCI (Arakawa et al., 2020; Nishiyama et al. 2020). These craters are particularly rich in boulders and this could reflect the subsurface structure of this region and/or crater formation process. In the Momotaro crater, for example, a large elongated boulder (~30 m long) is observed on the eastern rim with its longer side oriented toward the crater center; another elongated boulder occurs almost vertically with respect to the surface (Figure 2f), which could be the results of an intense boulder reorientation during the impact event. Very large (30-50 m), flat and bright boulders are seen on the southern crater wall of Kibidango. Along with the 70-m wide, 10-m thick flat block located at 100 m west of Kibidango, the high abundance of large boulders is consistent with the boulder-rich nature of the high latitude reported by Michikami et al. (2019). On the surface of the flat boulder lies fine-grained material suggestive of ejecta from some craters.

The eastern part of Momotaro's floor is also particularly rich in several-to-10-m angular boulders with a color similar to that of large bright boulders in Kibidango. The western half in contrast shows finer boulders of a redder spectral slope (Sugita et al., 2019). Various interpretations are possible to account for the particular high boulder number density. The boulders originally on/under the surface could have been excavated or even crushed upon the impact that made Momotaro; the impact that made overlying Kibidango could have broken the original rim of Momotaro, scattering the bright boulders into its floor as ejecta, given the resemblance of the color of boulders; an exposure of subsurface boulders; a result of mass movement from the equator; or immature boulder breakdown due to thermal fatigue. A smaller crater (~20 m) overlies the northern rim of the Momotaro crater (Figure 2e). Its smooth interior suggests that the subsurface of the Momotaro's rim (~2 m), which is potentially ejecta deposits, is made of fine-grained material, in contrast to Momotaro-crater's interior.

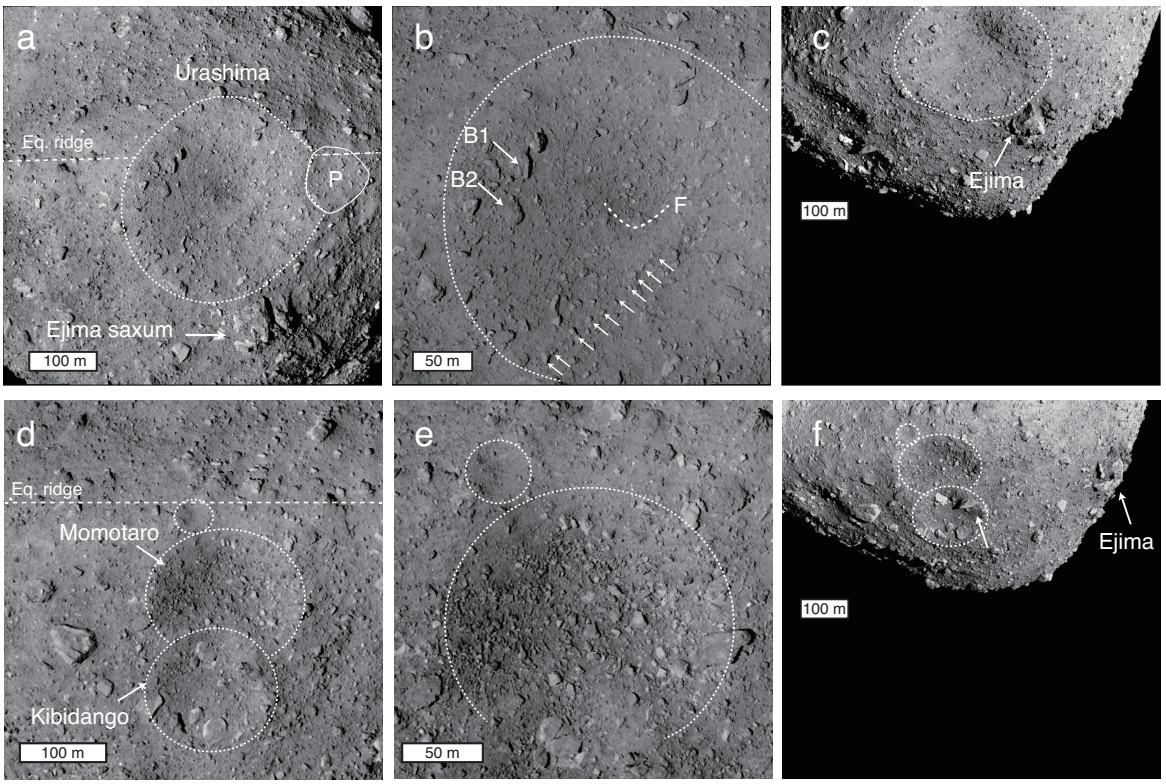

Figure 2. (a) Geological context of the Urashima crater. The northern rim crosses the equatorial ridge. The eastern rim is punctuated by a plateau ("P"). Ejima saxum is located just outside the southern rim (hyb2_onc_20180801_162509_tvf_l2d). (b) Urashima in close-up. Finer materials partially cover large (~20 m) boulders (B1, 2) on their high-geopotential side, a feature suggestive of mass flow into the crater. Dashed curve "F" shows the front of the putative slumping. A series of short arrows indicate possible linear streak composed by linearly aligned boulders (hyb2_onc_20181003_142939_tvf_l2d). (c) Urashima crater and the Ejima boulder (white arrow) showing the flat flank (hyb2_onc_20180301_080258_tvf_l2d). (d) Geological context of the Momotaro and Kibidango craters (hyb2_onc_20180801_170957_tvf_l2d). (e) Close-up of Momotaro's floor, which is very rich in angular boulders (hyb2_onc_20181004_062159_tvf_l2b) (f) Sharp elongated boulder sticking out at Kibidango's rim (white arrow). Note the very large flat boulders lying crater's southern rim (hyb2_onc_20190301_084153_tnf_l2d).

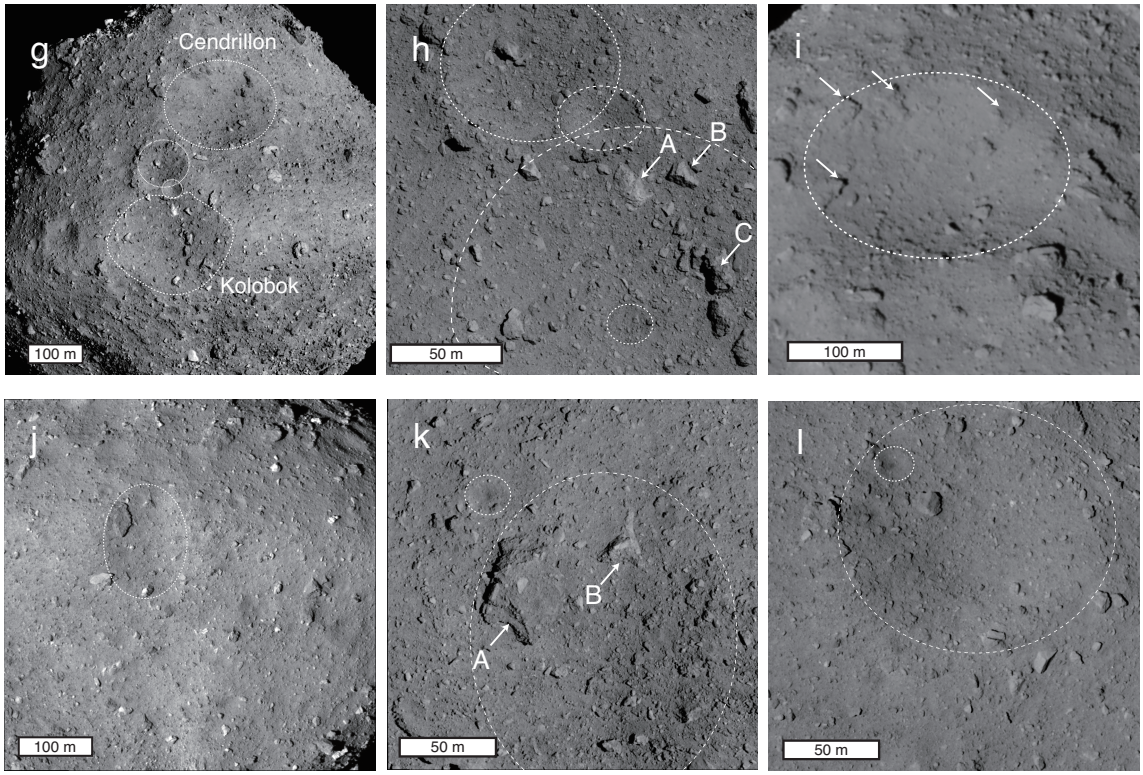

406

407 **Figure 2** (continued). (g) Geological context of the Cendrillon and Kolobok craters
408 (hyb2_onc_20190228_113636_tvf_l2b). (h) Northern part of Kolobok. White arrows indicate
409 angular boulders discussed in the text. Dashed circle in Kolobok shows the smaller crater on
410 the crater floor (hyb2_onc_20180720_090130_tvf_l2d). (i) Cendrillon crater with large
411 boulders on the rim (white arrows) (hyb2_onc_20190228_113636_tvf_l2b). (j) Geological
412 context of Kintaro (hyb2_onc_20180801_144909_tvf_l2d). (k) Kintaro's floor in close-up.
413 Prominent boulders ("A" and "B") lie in the crater. A smaller crater with dark center is on the
414 crater rim (smaller dashed circle) (hyb2_onc_20190404_220403_tvf_l2d). (l) Brabo crater. A
415 smaller crater with dark center is on the rim (smaller dashed circle).
416 (hyb2_onc_20181003_191510_tvf_l2d).

417

418 The *Cendrillon* crater (28°N, 6°W, 230 m) is the largest crater located outside the
419 equatorial ridge (Figures 2g, i). This crater provides critical hints on Ryugu's subsurface at a
420 middle-to-high latitude because the ridge is probably covered by thick materials transported
421 over the course of the surface evolution. The crater interior is smooth as a whole, but larger
422 (several to 15-m) boulders tend to occur on the southern wall. Portions of a few dark,
423 hummocky boulders are exposed on the northern half of the rim (~45°N). The surface texture
424 of the boulders resembles those of other hummocky boulders/massifs at similar latitudes of the

north hemisphere. The deep interior of Ryugu could be made of such hummocky boulders, which were too large to migrate to the equator even in the fast-spin period in the past. Spectrally, Cendrillon is one of the reddest craters on Ryugu (Table 2). If reddening is caused by space weathering, both the color of the crater floor and size suggest that this crater is one of the oldest on Ryugu.

The *Kolobok* crater (0.7°S, 330°E, 221 m) is a very boulder-rich, saddle-shaped crater on the equatorial ridge (Figures 2g, 2h). A number of 10- to 20-m angular boulders are scattered on the floor, which is consistent with the boulder-rich surface around the crater. A bright and mottled boulder (Sugita et al., 2019; Tatsumi et al., 2020) is exposed on the northern wall ("A" in Figure 2h). This boulder could have been excavated by an impact from subsurface since it is buried in the crater. Stereometric analyses indicate that the crater floor exhibits very rough and complex topography, most likely because numerous boulders hindered the crater excavation process. Crater #30 excavates the western floor (Figure 2h). The floor between the crater and the angular boulder ("C" in Figure 2h) is anomalously flat (Namiki et al., 2019; Sugita et al., 2019). This may be because of mass wasting from the equatorial ridge on the east, or burial by ejecta deposit from the crater. The area around Kolobok is one of the most heavily cratered regions on Ryugu (Hirata et al., 2020). Two craters are overlying Kolobok's northern rim (Figure 2h). Across the ridge to the south, two craters are also located just outside the southern rim. Such craters at different diameters provide a good sense of vertical boulder size sorting on Ryugu. For example, the largest Kolobok crater shows a greater number density of boulders both on the floor and on the wall, while other smaller craters (100 m and 35 m) near the Kolobok crater exhibit smoother floor with boulders only on their rims. Figure 2h shows that a number of boulders larger than ~10 m occur in Kolobok (D = 221 m), while crater #11 (D = 100 m) hosts only one such boulder and crater #41(D = 40 m) does not host any. Though some of the boulders could have been transported from the outside of the crater, this trend suggests that the large boulders occur in craters with a depth of >10 m, while smaller boulders are buried at shallower depth of only a few meters.

The *Kintaro* crater is located where the Tokoyo fossa crosses the equatorial ridge (Figures 2j, k). A remarkable 30 × 50 m, 10-m-high boulder is on the western wall. This boulder exhibits a very complex lithology, being a possible breccia of bright clasts embedded in darker matrix ("A" in Figure 2k). The boulder appears to have a layered structure as well. The top of the boulder is sloping towards the crater center, suggesting that it sits on the crater wall rather than being buried in the ground. This boulder may have been exposed upon the crater-forming

impact given Ryugu's microgravity condition, as observed on the SCI experiment (Arakawa et al., 2020). If this extremely large boulder was excavated from the ridge upon the Kintaro-forming impact, the boulder should have been transported to the subsurface of the ridge before the impact, when the ridge was being formed. This scenario requires a ridge formation process that can transport a boulder as large as ~50 m to the equator. The breccia-like texture of this boulder suggests a low mechanical strength, which also has implications for the transportation mechanism. A sharp, triangular boulder is buried at the crater floor ("B" in Figure 2k). A small crater that is located just 30 m northwest of the crater rim (#69, 14 m) exhibits a smooth floor with a dark center, which is commonly observed in this crater size range. Such a dark center could reflect the property of the material exposed/produced at the crater center, such as highly porous materials (Sakatani et al., in revision).

The *Brabo* crater (3°N, 230°E, 142 m) is located at the approximated center of the western bulge (Figures 2l) and is the largest crater on this hemisphere. This crater is comparable to the Momotaro and Kintaro craters in terms of its size and the distance from the equator, but its interior is much smoother than those craters. This is consistent with the lower boulder number density of the western bulge (Michikami et al., 2019). A prominent ~20-m angular boulder is seen on the northwestern floor. It is unclear if this boulder was excavated from the subsurface or was transported from another place on this asteroid. A smaller crater (#64, 17 m) excavates the northwestern wall. The interior of this crater is even smoother than Brabo's floor and its center is darker than the surrounding suggestive of a regolith property distinct from the surrounding materials, as is often observed on such 10- to 20-m sized craters.

In addition to the relatively obvious craters, some quasi-circular features (QCFs) are found on Ryugu. Figure 3 shows the crater candidate located at 31°S, 284°E (crater ID=80). This feature is outlined by a partially circular pattern formed by 5-10-m sized boulders stretching into the Tokoyo fossa. The diameter of the QCF is 112 m. Such a circular occurrence of boulders is also observed for other higher confidence craters (e.g., Figures 2h, l). The interior of this QCF is not necessarily smoother than the materials outside the candidates. If this 112-m QCF is a crater, then the boulders and materials filling these craters require efficient material transport or crater degradation processes. If we assume that this QCF had an original d/D of 0.1, a regolith layer thicker than 10 m would be necessary to fill up this crater. Based on the topography, Matsumoto et al. (2020) proposed that an irregular depression at ~15°N, ~45°E might be a highly degraded crater. However, adding this depression into the CSFD would not significantly change the implied age value. Besides this irregular-shaped depression, the QCFs

larger than 50 m are found only on the latitudes higher than 30°. This could be an observational bias because most of the high-resolution observations were conducted from Ryugu's approximate equatorial plane, but the facts that the craters are less obvious in the higher latitudes and the crater number density itself is lower there (Hirata et al. 2020) suggest higher crater degradation rates at the higher latitudes, or different surface properties, such as cohesion and boulder number density. While further study is needed to address this issue, we hypothesize that this latitudinal dependence may result from fast resurfacing processes or mass movement at high latitudes.

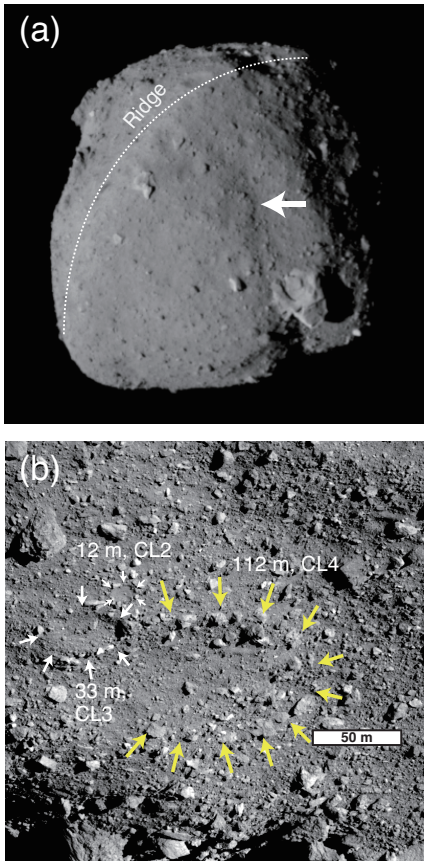

Figure 3. Example of a quasi-circular feature (crater candidate ID 80, CL 4). (a) Geologic context of the QCF (white arrow) (hyb2_onc_20180824_094938_tvf_l2d), (b) Close-up of the QCF (yellow arrows) and two smaller craters (ID = 88, CL3; ID = 96, CL2) located nearby (hyb2_onc_20190425_025446_tvf_l2d).

3.3 Crater morphology at different sizes

As seen in the previous section, craters on Ryugu have different morphological properties (e.g., floor, infilling, rim, boulders) at different size ranges. First, the craters larger than 100 m (Figures 4a-c) often contain a number of >10-m angular boulders. Such large boulders tend to lie on the crater rim, forming a circular pattern outlining the crater. Some of these boulders are partially buried by finer materials. A few prominent boulders often remain on the crater floor, too. Some of such intra-crater boulders were probably exposed by impact excavation as observed by the SCI impact experiment (Arakawa et al., 2020). Crater interiors exhibit a complicated and hummocky morphology, but generally smoother infilling material occurs while sometimes punctuated by large angular boulders. Craters on the equatorial ridge have saddle-shaped floors as shown in the significantly different east-west and north-south crater cross sections (Noguchi et al., 2021), presumably due to the original topography. Urashima and Kolobok craters overlap the ridge, indicating that the equatorial ridge is older than these craters. Some craters exhibit raised rims, suggesting gravity-controlled cratering on Ryugu (Sugita et al., 2019), which is consistent with the results from the SCI experiment (Arakawa et al., 2020). These large craters exhibit conical shapes rather than simple bowl shapes (Namiki et al., 2019). While the ejecta from the artificial crater was darker than the surrounding surface by ~20% (Arakawa et al., 2020), no obvious ejecta blankets or rays were found around the natural craters.

Craters with the diameter of 20-100 m (Figures 4d-f) tend to have smoother floors than larger craters, with less abundant boulders. Their floors are generally lacking boulders compared to the surface around the craters, a feature consistent with smaller craters described below. Some craters of ~20-30 m in diameter exhibit dark centers. Interpretations of the different albedo include different grain sizes, formation of a central pit, degree of compaction, freshness of the material, or crushed dark boulders. It might also be related to dark and fine material lofted upon Hayabusa2 touchdown (Morota et al., 2020).

Craters smaller than ~20 m (Figures 4g-i) are characterized by areas smoother than those of larger craters. Craters smaller than 10 m (Figure 4i) are mainly identified as a contrast in textures: smooth circular interior and rougher exterior, while it is difficult to determine if they have any bowl-like depression. This texture can be interpreted that the boulders were removed from the surface, creating a circular feature of smooth appearance outlined by apparently unaffected boulders. The boulders that have been at the impact site were likely either ejected or pulverized.

Table 3 summarizes the observations: large craters (>100 m) on Ryugu are circular or saddle-shaped depressions hosting numerous >10 m boulders. They exhibit complex floor morphology. This could be due to interaction with original asteroid topography and buried boulders. Small craters (< 20 m) are smooth circular features lacking in boulders than their exterior. Craters of ~50 m show intermediate features: smoother interior than exterior and simpler floor morphology than largest craters. The general trend between boulder number density and crater size (Watanabe et al., 2020) is observed, which is very similar to that observed for Bennu (Walsh et al., 2019; Bierhaus et al., 2019). Compared to another rubble-pile asteroid Itokawa, where crater candidates are shallow and ambiguous depressions lacked in raised rims, the craters on Ryugu are much more distinct and sometimes exhibit raised rims.

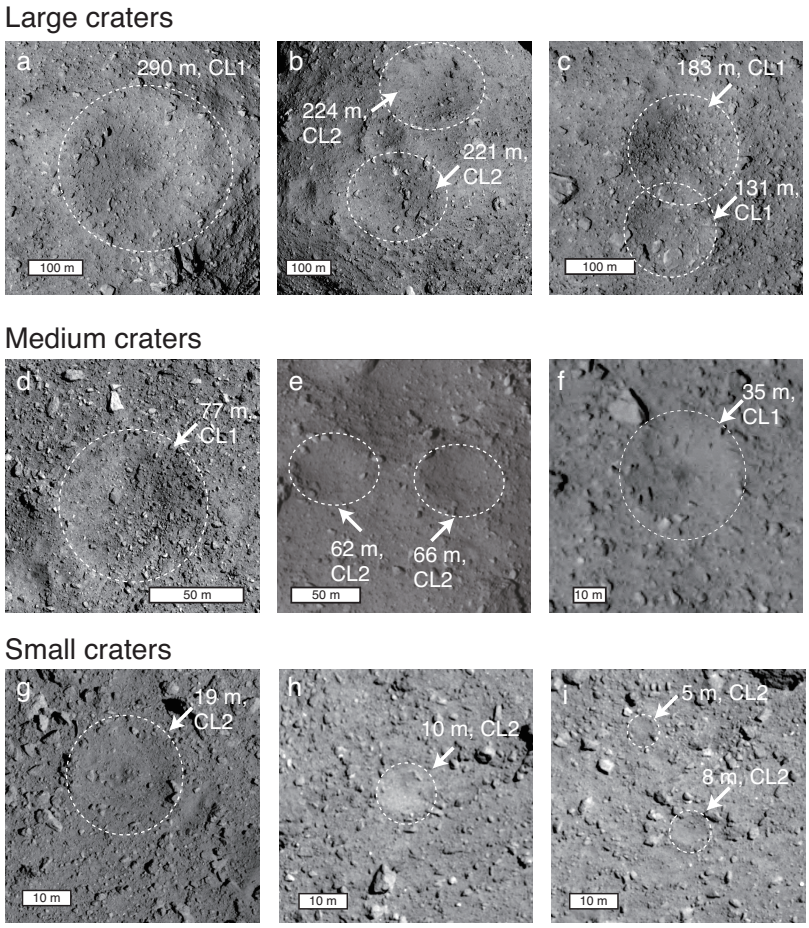

Figure 4. Morphology of craters on Ryugu at different size domains. (a-c) Large craters (D > 100 m), typically associated with large angular boulders on their floors. (d-f) Medium-sized craters (20-100 m), circular depressions outlined by boulders. (g-i) Small craters (< 20 m), characterized by circular features with a texture smoother than crater exterior. (a) Crater ID = 1 (Urashima), D = 290 m, CL 1 (hyb2_onc_20180801_162509_tvf_l2d). (b) ID = 2 (Cendrillon), 224 m, CL 2; ID = 3 (Kolobok), 221 m, CL 2

(hyb2_onc_20180801_170957_tvf_l2d). (c) ID = 4 (Momotaro), 183 m, CL 1; ID = 10 (Kibidango), 131 m, CL 1 (hyb2_onc_20180801_170957_tvf_l2d). (d) ID=16, 77 m, CL 1, (hyb2_onc_20190425_030150_tvf_l2d). (e) ID = 23, 66 m, CL 2; ID=24 62 m, CL 2, (hyb2_onc_20180801_151445_tvf_l2d). (f) ID = 46, 35 m, CL 1, (hyb2_onc_20181008_035159_tvf_l2b). (g) ID = 89, 19 m, CL 2, (hyb2_onc_20190516_024436_tvf_l2b). (h) ID = 77, *D* = 10 m, CL 2, (hyb2_onc_20190321_191258_tvf_l2d). (i) ID = 106, 8 m, CL 2; ID = 118, D = 5 m, CL 2. (hyb2_onc_20190321_191258_tvf_l2d).

Table 3. *Summary of characteristics of craters on Ryugu*

	Large craters	Medium craters	Small craters
Size range	> 100 m	20-100 m	< 20 m
Floor morphology	Circular or saddle-shaped depression; complex floor morphology	Simple depression	Smooth circular depression or texture; sometimes with dark center
Boulders	Numerous > 10-m boulders	Less boulders than exterior	Significantly less boulders than exterior

3.4 Implications for subsurface structure of Ryugu inferred from crater-floor morphology

The geomorphology of craters at different sizes provides clues on Ryugu's subsurface structure. Here we discuss the vertical structure of Ryugu's shallow subsurface by comparing the morphology of crater floors of different size ranges. Craters smaller than ~20 m exhibit smoother interiors compared to larger craters. It is unlikely that a crater-forming impact crushes all of the boulders on/below the surface to form the smooth floor because a number of intact large boulders are observed in larger craters. In fact, both the SCI experiment and laboratory studies show displacement of boulders in the craters rather than fragmentation of them (Arakawa et al., 2020; Tatsumi & Sugita, 2018), except for the boulder directly hit by the projectile. Thus, we interpret that the smooth crater floors observed for the craters with $D < 20$ m suggest that the crater-forming impact removes boulders on the surface, exposing finer materials just below the surface boulders or at very shallow (~2 m) subsurface (Figure 5).

Although a regional variation is observed in boulder number density (i.e., higher latitudes exhibit more boulders), the apparent richness of boulders in the craters larger than 50 m in turn implies that the finer material did not reach the depth of 5-30 m. The Kolobok crater region is a good example to explore the size sorting because three craters with different diameter occur in close proximity. The finer materials under the blocky surface could be the fragments of surface blocks produced by impact gardening and/or thermal fatigue. Alternatively, the smooth interior could be due to vertical size sorting processes on Ryugu.

Possible mechanisms for the size-sorting effect, in which larger boulders (several meters) remain on the very top surface, whereas smaller boulders (< 1 m) occur just below the surface, include regolith convection (Miyamoto et al., 2007), mass motion at the crater modification stage, surface material flows, and ejecta blanketing. Regolith convection is thought to be activated by seismic shaking (Yamada et al., 2016). Though the SCI experiment revealed low seismic efficiency at least for the impact that formed a 15 m crater (Arakawa et al., 2020; Nishiyama et al., 2020), the seismic energy deposited by a large-scale impact that would form a >100-m crater, needs to be evaluated. If granular convection takes place on Ryugu, this process would sort the size of particles because small particles can travel much more easily while larger rocks remain at the surface. Given the boulder-rich surface of Ryugu, large boulders buried under the surface might work as a wall of a convection cell. Although *v*-band images do not show clear features of ejecta around natural craters on Ryugu, the SCI experiment showed a clear ejecta blanketing process (Arakawa et al., 2020), implying that global ejecta blanketing can work as another sorting process. A possible explanation for size sorting during crater formation is that smaller particles are ejected more easily than larger particles: larger particles need higher kinetic energy and momentum to be ejected (Melosh, 1989). Also, smaller particles can also be blown off due to solar radiation pressure, solar winds, and other non-gravitational forces. Therefore, only larger boulders can come back to the surface of Ryugu. The thickness and deposition rate of ejecta on Ryugu should be addressed in a future study taking Ryugu's spin rate into account. The finer material inside small craters is also observed on Bennu (DellaGiustina et al. 2020). Other examples of size-sorting processes observed on asteroids include ponded deposits on Eros (Cheng et al., 2002). Possible processes forming such extremely fine deposits include electrostatic levitation of fine materials (Robinson et al., 2001) and seismic shaking (Veverka et al., 2001). Some craters on Itokawa also exhibit similar fine deposits on crater floors (Hirata et al., 2009). In contrast, natural craters on Ryugu do not show such ultra-fine deposits on their floors.

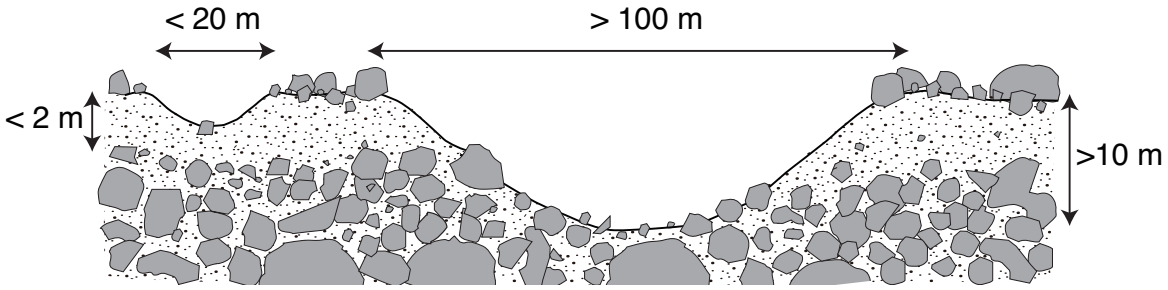

Figure 5. Cross section of Ryugu's shallow subsurface inferred from crater morphology. A few-m-thick layer of fine-grained material is inferred between the boulder-rich surface and several-m deep subsurface.

4 Crater chronology of Ryugu

In contrast to the previous section, which focused on crater morphology, this section focuses on the history of Ryugu based on crater chronology. In section 4.1, we report the crater number density of each unit and discuss the stratigraphic relations on Ryugu. In section 4.2, the crater size-frequency distributions of different regions on Ryugu are reported. The model ages are derived with isochron fitting. In section 4.3, we discuss the regional difference of the model ages. In section 4.4, the geologic history of Ryugu is reconstructed based on the age data and their interpretations. The ages of Ryugu as a near-Earth asteroid (after being decoupled from the main belt) and as a main-belt asteroid are discussed. In section 4.5, the spin evolution and YORP effect are discussed based on the chronology data.

4.1 Relative ages based on stratigraphic relations and crater number density

The stratigraphic relationships among the different units are not necessarily clear on Ryugu because of the very limited number of cross-cutting features. The equatorial ridge at least predates the largest craters that cut the ridge (Urashima, Kolobok, Momotaro, and Kintaro), suggesting that the ridge is the oldest structure on Ryugu. The stratigraphic age of the trough relative to the ridge, eastern hemisphere, and western bulge is unclear. The trough does not appear to cut the ridge based on the topography. The trough outlines both hemispheres without clear crosscutting features. The ridge formation could have been ongoing when the western bulge formed because the equatorial ridge running on the western bulge is almost perfectly circular as well (Watanabe et al., 2019). The Brabo crater, the largest one on

the bulge, should be younger than the western bulge formation. The lack of morphological features representing stratigraphic relations underlines the importance of crater number density measurements.

Crater number densities provide an independent measure of relative age for geologic units because they are independent of chronology models. Thus, before applying the crater-chronology models, the crater number densities at different units and diameter ranges were measured (Table 4). Table 4 shows crater number densities at different diameter bins to address the processes potentially observed in different spatial/time scales. For example, crater statistics at >100 m in diameter suggests different resurfacing history that reaches > 10 m in depth between the eastern hemisphere and western bulge. The crater records at 50-100 m show the transition of isochrons, which suggest a resurfacing event in a short time period (see section 4.2). The similarity of crater number density N (D > 10 m) among multiple units suggests that the timescale of erasing 10-20 m craters does not differ between the eastern hemisphere and western bulge. This is potentially because of the ongoing surface processes, such as surface flow.

The equatorial ridge shows the highest crater number density $N(D>10$ m) among the units addressed in our study, although statistical significance is sometimes poor due to the small number of craters on Ryugu. The crater number density of the equatorial ridge on the eastern hemisphere is slightly larger than that of the ridge on the western bulge at an insignificant level. The crater number density on northern and southern hemispheres are statistically equivalent, but the regions at latitudes higher than 10° have significantly smaller crater number density than the equatorial ridge.

Table 4. *Crater Number Density at Different Units*

Unit	Area (km^2)	$N(D > 10$ m) (km^{-2})	$N(D > 20$ m) (km^{-2})	$N(D > 50$ m) (km^{-2})	$N(D > 100$ m) (km^{-2})	Model age (Ma)	Diameter range (m)
Eastern hemisphere	1.772	29.3 ± 4.1	26.0 ± 3.8	11.9 ± 2.6	5.1 ± 1.7	4.89 ± 1.6	60-100 m
						11.7 ± 4.2	>120 m
Western bulge	0.932	25.8 ± 5.3	17.2 ± 4.3	8.6 ± 3.0	1.1 ± 1.1	2.07 ±0.92	> 50 m
Equatorial ridge	0.578	41.5 ± 8.5	32.9 ± 7.5	17.3 ± 5.5	6.9 ± 3.5	22.5 ± 14	> 120 m
East-EQR	0.339	44.2 ± 11.4	38.3 ± 10.6	20.6 ± 7.8	5.9 ± 4.2		

West-EQR	0.239	33.5	±	11.8	20.9	±	9.4	8.4	±	5.9	4.2	±	4.2		
Latitude >10°	2.13	28.0	±	5.1	22.4	±	4.6	10.3	±	3.1	2.8	±	1.6		
North hemisphere (>10°N)	1.07	24.5	±	4.8	20.8	±	4.4	8.5	±	2.8	3.8	±	1.9		
South hemisphere (>10°S)	1.06	26.3	±	3.5	21.6	±	3.2	9.4	±	2.1	3.3	±	1.2		
Fossae	0.18	16.7	±	9.6	11.1	±	7.9	0.0	±	0.0	0.0	±	0.0		
Global	2.70	29.3	±	3.3	24.1	±	3.0	11.1	±	2.0	4.1	±	1.2	8.15 ± 2.5	>100 m

Note. Errors were calculated by $\pm N^{1/2}/S$, where N is the cumulative number of craters and S is the area of individual units. The Kintaro crater was not assigned to Eastern hemisphere nor Western bulge because it is located at their boundary. The data from the global crater survey were used. Absolute model ages derived in section 4.2 and diameter range used for fitting are shown.

4.2 Crater model ages

The crater size frequency distributions are constructed based on the crater list on Table 2 and fitted with the MBA- and NEA-model functions (see section 2.4 for details). First, we use the NEA chronology function to derive the age that Ryugu spent in the near-Earth orbit. Then the CSFDs in different crater size ranges are measured.

Figure 6 shows CSFDs with the global observation data and those with higher-resolution SCI-crater-survey images. The shape of the CSFD is consistent with that obtained from a global crater catalogue at >30 m, with the crater number density twice as high as that of the global CSFD. This higher crater number density is because the SCI-crater-survey operation was carried out at a region that hosts craters more than Ryugu's global average (Figure 1). The CSFD obtained for the SCI-crater search region exhibits a transition of isochrons at $D \sim$ 10-15 m (Figure 6). The transition was not reported in the previous studies because of the limitation of image resolution (0.5 m/pix). The higher-resolution images (0.2 m/pix) revealed the presence of the upturn in the CSFD in this diameter range and the deviation from the crater production function (i.e., paucity of small craters) at craters smaller than 10 m. Secondary craters will not contribute to the CSFDs because the speed of ejecta that would hit the ground is limited to less than the escape velocity of 0.27 m/s. Such a slow impact would not form an apparent crater on the ground covered with the boulders, when the target disruption

energy Q_D* is taken into account. The younger isochron at D = 10-15 m corresponds to 0.22 ± 0.05 Ma with the MBA model (Figure 6a), while it yields 7.2 ± 1.6 Ma with the NEA model (Figure 6b). The isochron is consistent with that of "blue craters," presumably fresh craters which are interpreted to be formed in the near-Earth orbit (Morota et al., 2020) (Figure 6b). The CSFDs for the global observation data yielded 8.1 ± 2.5 Ma at D > 100 m and 4.1 ± 1.1 Ma at 70-80 m with the MBA model (Figure 6a).

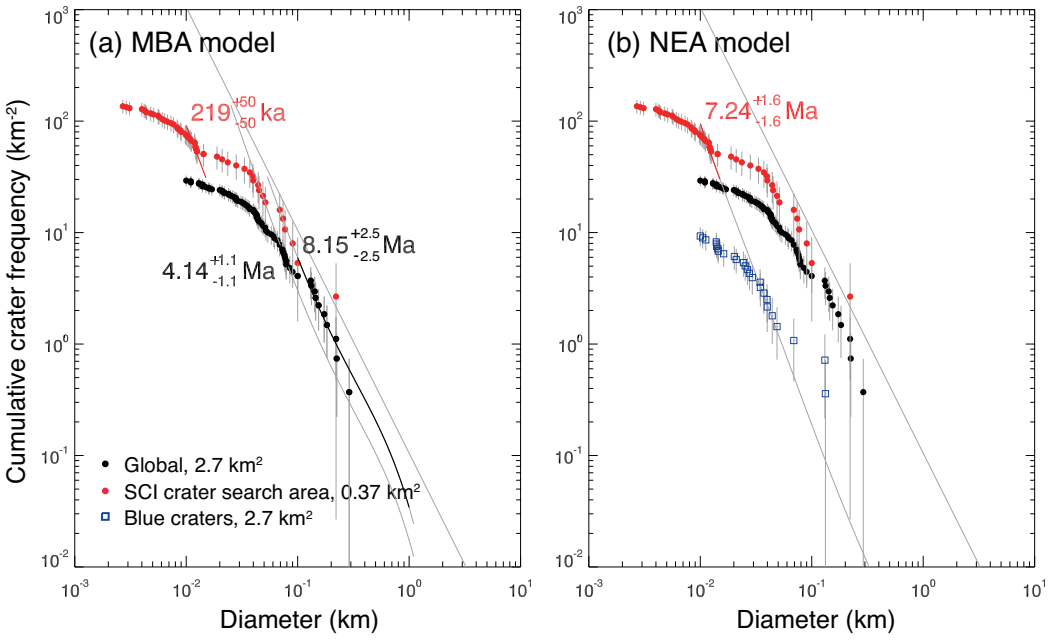

Figure 6. Crater size-frequency distribution obtained with the global observation campaign (black circles) and SCI crater-search operation carried out from a lower altitude (blue circles). The CSFD for "blue craters" (Morota et al., 2020) is shown in open squares. Data fitted with (a) MBA model and (b) NEA model. Age errors are derived from isochron fitting.

Isochron fitting for the large craters on different units (> 120 m for EH and EQR, > 50 m for WB) yielded the absolute model ages of the equatorial ridge, eastern hemisphere, and western bulge as 23 ± 14 Myr, 11.7 ± 4.2 Myr, and 2.1 ± 0.9 Myr, respectively (Figures 7a, b). Here we report MBA model ages because the craters were most likely formed in the main belt: if these craters were formed in the near-Earth orbit, the surface of Ryugu would be ~30 times older, which is too long for Ryugu to stay as a near-Earth asteroid in a typical dynamical timescale of ~40 Ma (*Michel and Delbo* 2010). The eastern and western ridges were statistically equivalent given the error bars.

The CSFD of the western bulge shows no evidence of isochron transition at $D > 40$ m, suggesting a simple bombardment history in the main belt after the resurfacing of craters of all diameter ranges. In contrast, the CSFD of the eastern hemisphere using the global observation data can be divided into two regimes. The craters of 50-100 m in diameter were well fitted by an isochron of 4.9 ± 1.6 Myr (MBA model), while those larger than 120 m yielded the age of 11.7 ± 4.2 Myr (MBA model) (Figure 7b). However, the crater data reconstructed with the SCI crater-search images did not show the transition of the isochron on the eastern hemisphere.

The CSFD for the *Tokoyo* and *Horai* fossae coincides with that for the western bulge (Figure7b) although the statistics is poor because the number of craters was only three.

The CSFDs constructed for the southern and northern hemispheres outside the ridge show that the crater data on the latitudes higher than 10° do not follow the standard production function (Figure 7c).

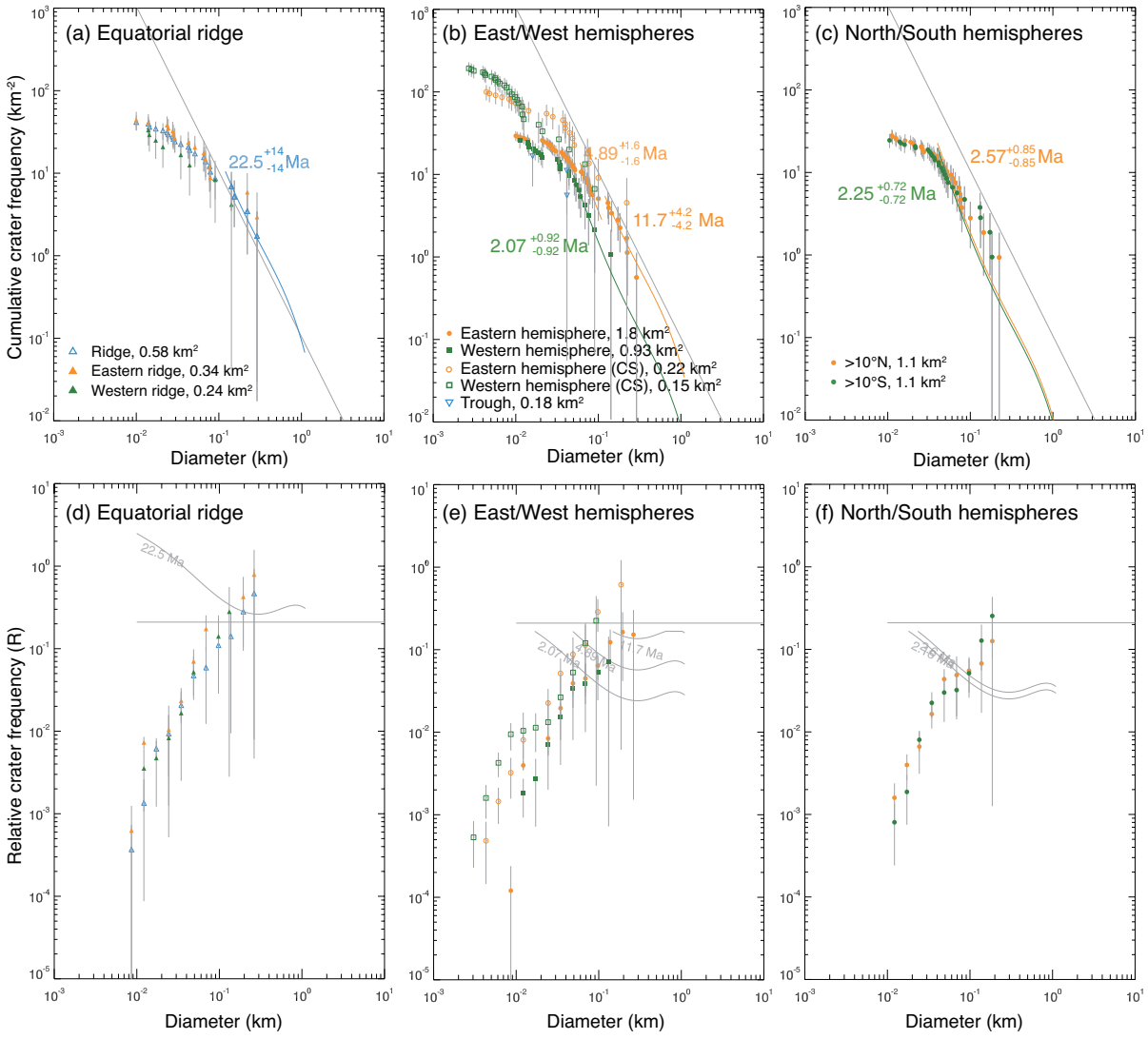

Figure 7. Crater size frequency distribution and isochron fitting for the craters on (a) the equatorial ridge (10°N-10°S), (b) east/west hemispheres and fossae constructed from global observation and higher-resolution SCI crater-search (CS) images, and (c) higher latitudes (10°N-90°N and 10°S-90°S). Gray lines show the empirical saturation level. R-plots for the same data (d, e, f).

4.3 Regional difference of ages and possible reasons

We now discuss the ages of the individual units on Ryugu using the age data obtained from Figures 6 and 7. Here, a near-Earth asteroid tends to be more exposed to impacts when it reaches the aphelion that is near or in the main belt (O'Brien and Greenberg, 2005; Sugita et al., 2019). The bombardment in the main belt continues until the orbit of the NEA is decoupled from the main belt. Thus, the ages of 7 Ma (NEA chronology model) and 0.2 Ma (MBA chronology model) correspond to the earliest and latest timing (upper and lower age limits) when the asteroid was decoupled from the main belt, respectively (Figure 6). If the former is the case, the 7.2 ± 1.6 Myr period spent in near-Earth orbit should be added to the main-belt model ages.

First, we compare the model ages in the latitudinal direction. The equatorial ridge is the oldest structure on Ryugu, as suggested in Table 4. The isochron indicates that the asteroid spent 23 ± 14 Myr in the main belt (Figure 7a). For the early decoupling scenario, in which 7 Myr spent in the near-Earth orbit (Figure 6b) is added to the main-belt ages, the ridge was formed 30 Myr ago while Ryugu was rotating more than twice as fast as it is now (Watanabe et al., 2019). The craters larger than 100 m might have reached the empirical saturation level, and therefore the ridge could have been even older than 30 Ma. Nevertheless, the close proximity of large craters on Ryugu, such as Momotaro and Kibidango, suggests that obliteration/modification of preexisting craters by seismic shaking is inefficient on Ryugu and thus crater saturation level could be higher on this asteroid. Despite the hemispherical resurfacing on the western bulge (discussed in the following paragraph), the crater number densities of the eastern and western ridges were statistically equivalent (Figure 7a). This result is a constraint for the type and magnitude of the resurfacing process. The nonstandard crater population on latitudes higher than 10° supports a continuous, gradual crater obliteration process rather than a single resurfacing event that would result in a transition in isochrons. One candidate process that accounts for the lack of craters only at middle-to-high latitudes would

be mass movement induced by evolving geopotential. The preservation of craters on the ridge suggests that the mass motion did not reach the ridge to erase the craters there, possibly because of the lack of movable material or because of geopotential barriers. The mass and intensity of the latitudinal mass movement would be the key to addressing the crater population at the middle-to-high latitudes. Another possible mechanism to make the latitudinal crater density variation is that craters did not occur at the high latitudes as much as on the equator. Such crater depletion on the higher latitudes could be because of different surface properties between the equatorial region and the higher latitudes (e.g., cohesion, boulder size, boulder number density). Although the SCI impact experiment revealed gravity-controlled cratering on the ridge (Arakawa et al., 2020), further quantitative studies on armoring and cohesion are needed to address the lack of craters on the higher latitudes.

Next, we compare the CSFDs of the eastern hemisphere and western bulge (Figure 7b). First, the best-fit isochrons (i.e., those with diameter > 60 m for EH and that of > 50 m for the WB) reveal that the western bulge possesses significantly smaller number of craters than the eastern hemisphere, indicating the presence of dichotomy in terms of crater number density. Deformation analyses provide one possible mechanism for this hemispherical, semi-global resurfacing event through the relaxation of stress in the asteroid: the imperfect axisymmetric shape of Ryugu may have induced a deformation mode that resurfaces only one side of the asteroid (Hirabayashi et al., 2019). In other words, the western bulge was resurfaced due to mass movement driven by structural deformation. Note that we do not rule out any deformation mode: a landslide or internal deformation. It is challenging to identify the source impact or events that induced the global deformation in a reliable way, since any perturbation could have induced such a relaxation (Hirabayashi et al., 2019). Nevertheless, one possible candidate would be the Brabo crater, which is located at the center of the western bulge. If this is the case, the Brabo crater itself caused but survived the resurfacing event, a constraint on the scale and mechanism of the formation of the western bulge.

The transition of isochrons on the eastern hemisphere at 11.7 Ma (D > 120 m) and 4.9 Ma (D = 60-110 m, Figure 7b) suggests that the craters smaller than 110 m were obliterated ~5 Myr before Ryugu left the main belt (i.e., 5 or 12 Myr before the present with MBA/NEA models). If the depth-to-diameter ratio (d/D) of a fresh crater is 0.1 on Ryugu (Noguchi et al., 2021), materials up to 10-m thick would be needed to erase the craters smaller than 100 m. One possible source of such a large-scale resurfacing is the ejecta deposition and/or topographic diffusion by Urashima, the largest crater on Ryugu. In fact, the crater number density decreases

788 as crater location comes closer to the Urashima crater (Figure 8). For the ejected material to
789 cover 1-4 crater radii with the thickness of 10 m, for example, 50% of the volume of Urashima
790 crater needs to be deposited on the surface. This amount of material is comparable to the result
791 of a simple model calculation using the ejecta scaling rule (*Housen and Holsapple*, 2011), dry-
792 sand parameters, escape velocity of 0.275 m/s, as well as the *Z*-model (*Maxwell*, 1977), in
793 which approximately 80% of ejecta returns to Ryugu. The apparent lack of craters around
794 Urashima as compared to the Kolobok area (Figure 1) is consistent with this interpretation.
795 Although the seismic efficiency on Ryugu was found low by the artificial impact experiment,
796 the seismic shaking due to the Urashima-forming impact could also have degraded a number
797 of craters nearby because the seismic energy with this 290-m crater formation is still high
798 enough to induce acceleration greater than the gravity (Nishiyama et al., 2020). This hypothesis
799 is also consistent with the fact that the CSFD for the eastern hemisphere does not show the
800 transition of the isochron if constructed with the data from SCI crater-search campaign,
801 whereas the CSFD from the global observation campaign does. This difference can be
802 interpreted that the SCI crater-search area is far from the Urashima crater and its resurfacing
803 did not affect this area.
804

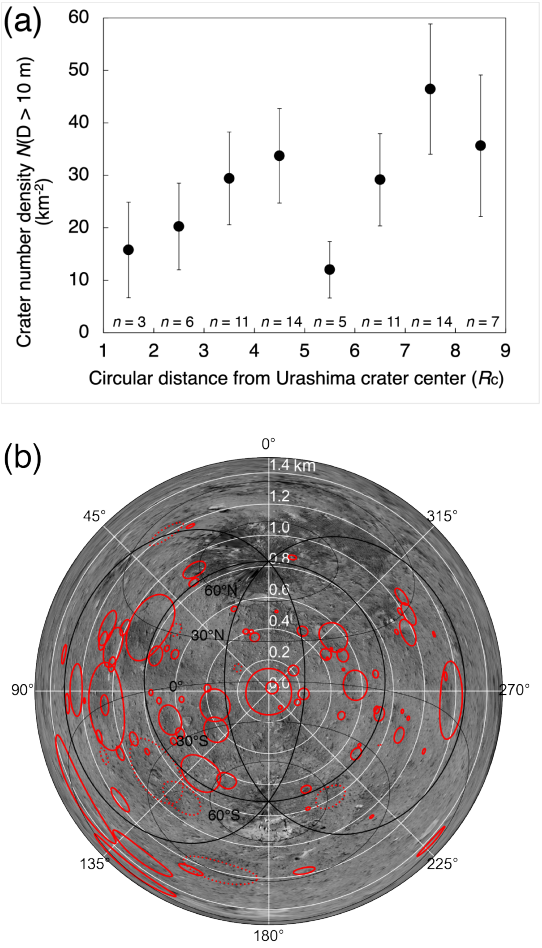

805

806 **Figure 8**. (a) Number density of craters larger than 10 m as a function of circular distance
807 from the Urashima crater (crater radius R_c). The numbers of craters in each bin (n) are also
808 shown. Note that the area of R_c = 5-6 includes both polar regions, where few craters are
809 found. (b) Distribution of craters around Urashima.

810

811 Finally, we found that the CSFD for the *Tokoyo* and *Horai* fossae coincides with that
812 for the western bulge (Figure7b). This result is important because no clear stratigraphic
813 relationships were found among the fossae and other units. Although the statistics are poor
814 because the number of craters is only three, this agreement strongly suggests that the fossae
815 were formed in association with the formation of western bulge 2 Myr (late decoupling model)
816 - 9 Myr (early decoupling model) ago. It is still unclear why the fossae are much bluer than the
817 western bulge, because the degree of space weathering should be comparable to each other.
818 One hypothesis is that the trough is even younger than the western bulge and occurred after
819 surface reddening process during Ryugu's orbital excursion 0.2-8 Myr ago (Morota et al.,
820 2020). If this is the case, the resurfacing on the trough could be a geologically very recent,

potentially ongoing process. As described in the previous paragraph, the two fossae outlining the western bulge are likely to have formed associated with a reshaping process of the western bulge. The significantly different crater ages between the eastern hemisphere and western bulge speak against the simple two-body merge scenario as the origin of the dichotomy: the two hemispheres underwent different geologic histories. Furthermore, the poorly preserved morphology of the putative crater at 15°N, 45°E (Matsumoto et al., 2020) does not seem to support the impact origin of the recently formed western bulge.

4.4. History of Ryugu revealed by cratering record

In this section, we summarize Ryugu's history from the top-shape formation to the present based on the crater population data. Because the age when Ryugu was decoupled from the main belt is sometime between 7 and 0.2 Myr ago, both early- and late-decoupling cases are described (Figure 9).

The precursor top shape (i.e., the equatorial ridge) developed by 23-30 Myr ago after the catastrophic disruption of Ryugu's immediate parent body (Figure 10). The crater record does not provide the time of the catastrophic disruption that formed Ryugu. If we assume that Ryugu's parent body is Eulalia or Polana, which experienced breakups 1500-3000 Myr ago (Bottke et al., 2015; Sugita et al., 2019), then Ryugu's current shape has to be formed in the last 1% of that time. This time scale suggests that Ryugu is likely multiple generations younger than, rather than is an immediate daughter asteroid of, these potential parent bodies. The age of the disruption will be revealed by radiometric dating of returned samples. As mentioned earlier, the spin period may have been as fast as 3.5 hr at this time to form and enhance the equatorial ridge (Watanabe et al., 2019; Hirabayashi et al., 2019), suggesting the long-term rotational evolution over the life of this asteroid. Because the age of 23-30 Myr is comparable to the dynamical lifetime of Ryugu, the top shape might have been a direct result of disruption (Michel et al. 2020).

While Ryugu was in the main belt, it experienced continuous impact cratering. The current topography of the eastern hemisphere formed 11-18 Myr ago. Statistically, the formation of the eastern hemisphere, as well as the original western hemisphere before the dichotomy formation, can be contemporary with the equatorial ridge (Figure 9). Nevertheless, one hypothesis to account for the apparent age gap between the ridge and the entire eastern hemisphere is that the craters at the high latitudes were erased as materials passed through the

region. Another possible reason for the ~12-Myr younger eastern hemisphere, which includes the areas at higher latitudes, is that craters did not occur at the high latitudes as much as on the equator possibly because of armoring effects or different cohesion, making the eastern hemisphere appear younger compared to the equatorial ridge.

The eastern hemisphere was resurfaced 5-12 Myr ago. This 10-m thick, hemispherical resurfacing event could have been caused by the formation of the largest crater Urashima, which would have obliterated preexisting craters on a part of the eastern hemisphere via ejecta blanketing and/or seismic shaking.

2-9 Myr ago, the western bulge formed presumably with the fossae. The bulge could have been formed by the relaxation of stress in the asteroid that causes a hemispherical mass movement. This event might have modified the equatorial ridge in a way that erases craters at an insignificant level as well (Figure 7a). This resurfacing event occurred >20 Myr after the original ridge formation (Figure 7a). After this event Ryugu's spin rate slowed down to the current value of 7.6 hr likely due to the YORP effect.

Between 0.2 and 7 Myr ago, Ryugu was decoupled from the main belt to the near-Earth orbit. This age is reasonable because it is substantially younger than the typical dynamical lifetime of 40 Myr that an asteroid spends in the near-Earth orbit (Michel and Delbo, 2010). The contrast of colors of some craters on Ryugu suggests that Ryugu's orbit once was much closer to the Sun than it is now, where the asteroid would have experienced surface reddening (Morota et al., 2020). Then, Ryugu changed its orbit to the current one.

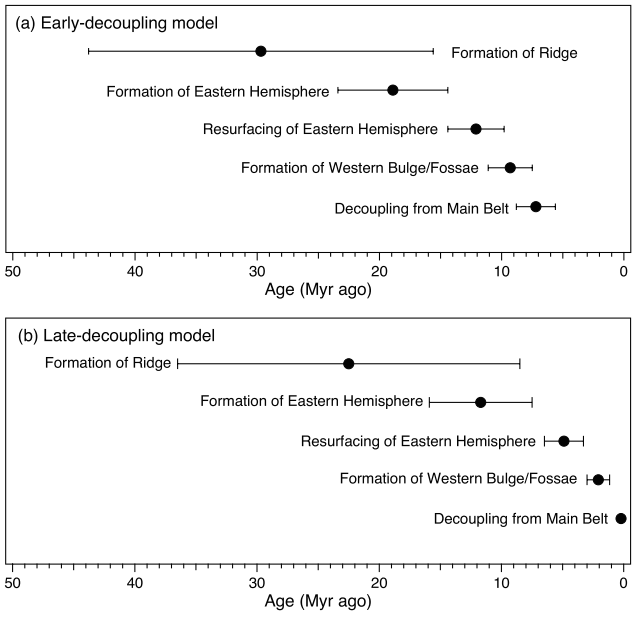

Figure 9. Ages of geologic events on Ryugu. Two scenarios are illustrated: (a) Ryugu was decoupled from the main belt 7 Myr ago and became a near-Earth object (NEA chronology model); (b) Ryugu was decoupled from the main belt 0.2 Myr ago (MBA chronology model). Error bars show the uncertainty of the absolute model ages.

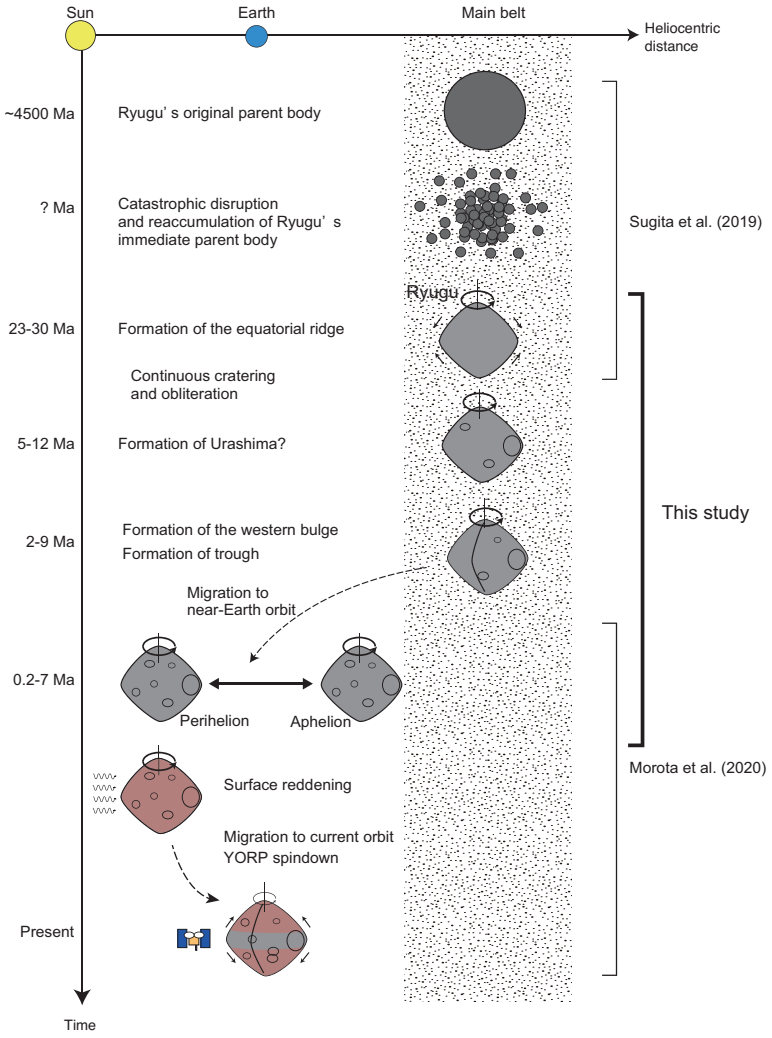

Figure 10. Evolution of Ryugu as revealed by this study. This study revealed the geologic history from the formation of the top-shape, to the migration from the main belt to the near-Earth orbit. Parent-body processes were discussed by Sugita et al. (2019); orbital excursion and surface reddening are after Morota et al. (2020).

The most recent, potentially ongoing geologic activities on Ryugu include turnover of regolith or pebbles. The residence time of individual grains shallower than ~1 m can be

889 estimated from the intersect of crater distribution and model isochrons at a crater diameter of
890 10 m (Sugita et al., 2019). Figure 11 shows the CSFDs of Ryugu and isochrons for the MBA
891 and NEA models. The expected age of the top 1-m layer differs between the models. Thus, the
892 galactic cosmic-ray exposure ages of returned samples, which would record the irradiation
893 history of ~1 m beneath the surface (Nagao et al., 2011), can be used for discriminating the
894 models and reconstructing the geologic history of Ryugu. The cosmic-ray exposure age of
895 returned samples would be 10-100 ka for the late-decoupling case. In contrast, the exposure
896 age would be ~1 Ma for the early-decoupling model, because Ryugu spent ~7 Ma in the NEO,
897 where much fewer meteoritic impacts take place.

898

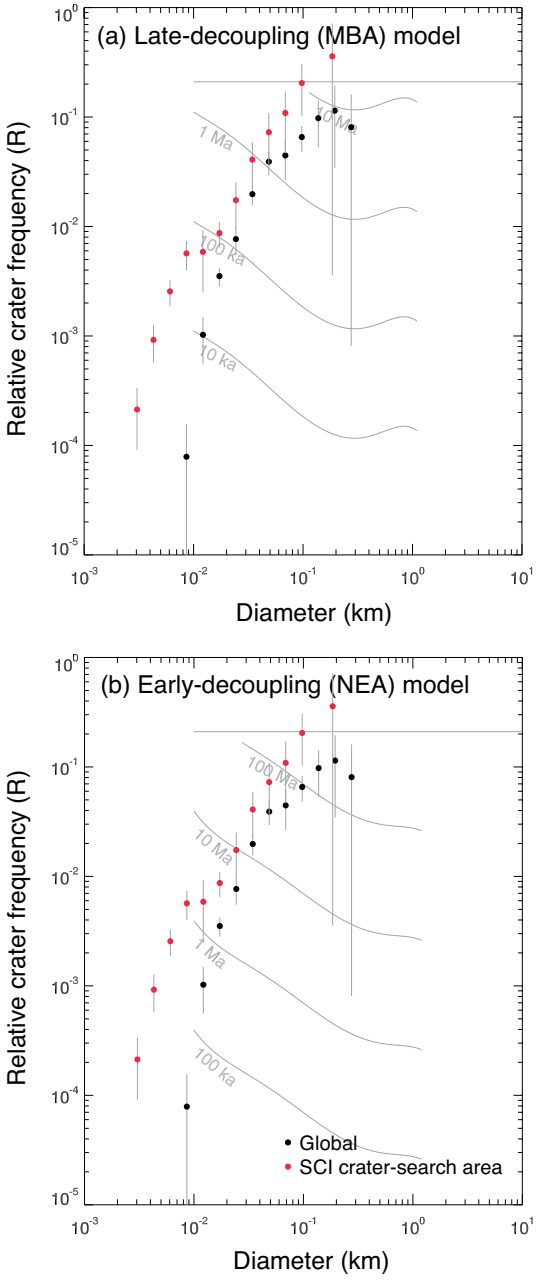

899

Figure 11. Crater size-frequency distribution and model isochrons with (a) main-belt asteroid model and (b) near-Earth asteroid model. The MBA and NEA models correspond to late and early decoupling, in which Ryugu was decoupled from the main belt 0.2 Myr ago and 7 Myr ago, respectively (Figure 6). The intersects of CSFDs and model isochrons yields approximate residence time at the depth of crater excavation and could be compared with the cosmic-ray exposure age of returned sample. Horizontal line shows the empirical saturation level.

4.5 Implications for spin-state evolution

Our crater chronology data can also be used for determining the timescale of the spin-state evolution on Ryugu because its spin period must have been 3.5 hr (Watanabe et al., 2019; Hirabayashi et al., 2019) when the western bulge formed as a result of the asymmetric deformation. The spin rate could be altered by the YORP effect and impact cratering processes. Mass ejection was also considered to be another contributor, but recent study showed that it might be negligible for Bennu (Scheeres et al., 2020). If the western bulge of Ryugu developed 2 or 9 Myr ago (Figure 7b) when the spin period was 3.5 hr, the average YORP deceleration rate is 1.8×10^{-6} or 4.1×10^{-7} deg day^{-2}, respectively. These values are consistent with the current deceleration rate derived from the shape model of Ryugu (1.3×10^{-6} deg day^{-2}, Kanamaru, 2020). For Bennu, light curve observations showed that the spin acceleration driven by the YORP effect is $(2.64 \pm 1.05) \times10^{-6}$ deg day^{-2} (Nolan et al., 2019). The magnitude of the YORP effect strongly depends on the local topography of individual asteroids (Statler, 2009). We can nevertheless estimate the timescale of the YORP effect on Ryugu by that of Bennu, with a simple conversion of the asteroid dimensions. The timescale of angular velocity (ω) change due to the YORP effect is $\dot{\omega} = \tau/I \sim 1/A^2$, where τ is the torque induced by the YORP effect, I is the moment of inertia, and A is the diameter of an asteroid. Here, $I \propto A^5$ and $\tau \propto A^3$. Considering that the bulk density and the shape are similar for both Ryugu and Bennu, the equivalent diameters of Bennu (~535 m) and Ryugu (870 m) give the YORP timescale of Ryugu ~0.38 times that of Bennu, or $(1.0 \pm 0.4) \times10^{-6}$ deg day^{-2}. The magnitude of this value, which is converted from Bennu's observed spin-up rate, is consistent with the spin-down rate obtained from crater chronology for Ryugu within a factor of 3. Despite the strong local-topography dependence, the agreement of these YORP rates indicates that the magnitude of the YORP effect observed for Bennu is sufficient to account for the spin rate change of Ryugu. In addition, the agreement of the YORP timescales in turn suggests that western bulge was resurfaced 0.2-7 Myr ago when Ryugu was spinning approximately twice as fast as it is now.

5 Conclusions

In this study, we reported the morphology of craters on Ryugu and used the crater population to decipher the geologic history of this C-type, rubble-pile asteroid. We used the high-resolution images obtained by the telescopic optical navigation camera on board the Hayabusa2 spacecraft. Our observations revealed that the abundant boulders on/under the surface of Ryugu affect crater morphology. For example, the craters exhibit relatively simple circular depressions, which was not the case for the rubble-pile asteroid Itokawa. The craters on the equatorial ridge show saddle-shaped floors due to the original, pre-impact topography. The craters are typically outlined by the circular pattern of boulders remaining on the rim. Large craters (diameter >100 m) host abundant and sometimes unproportionally large boulders on their floors. In contrast, small craters (<20 m) are characterized by much smoother circular floors in the middle of the boulder-rich surface of Ryugu. Such small craters also tend to have dark centers, of unclear origin. The correlation between crater size and boulder number density, which was also observed on Bennu, suggests the presence of processes that sort the boulders by size in the shallow (a few m) subsurface.

Furthermore, the crater size-frequency distributions (CSFDs) of different regions on Ryugu revealed the complex geologic history on this only 1-km asteroid (Figure 10). Our crater counting analyses and the crater chronology model for Ryugu indicate that Ryugu was transferred to a near-Earth orbit and decoupled from the main belt 0.2-7 Myr ago. The galactic cosmic-ray exposure ages of returned samples would be used for constraining the time when Ryugu was decoupled from the main belt: the ages should be ~1 Ma for the early-decoupling model (Ryugu spent 7 Myr in NEO), while they should be 10-100 ka for the late-decoupling scenario (Ryugu spent 0.2 Myr in NEO). Taking the period Ryugu spent in the near-Earth orbit into account, the equatorial ridge is the oldest structure of Ryugu and formed 23-30 Myr ago. Ryugu was then partially resurfaced possibly by the impact that formed Urashima at 5-12 Ma, followed by a hemispherical resurfacing event that formed the western bulge at 2-9 Ma. The crater number density on the trough was comparable to that on the western bulge, suggesting that Tokoyo and Horai fossae were formed associated with the resurfacing of the western bulge 2-9 Myr ago. Deformation analyses conducted by previous studies suggest that such a hemispherical resurfacing could have been caused by the relaxation of stress in the asteroid, providing a mechanism that accounts for the east-west dichotomy of Ryugu. The spin rate of Ryugu was then slowed down plausibly due to the YORP effect, because the size-corrected

timescale for the spin-down of Ryugu is comparable to the YORP spin-up timescale measured for Bennu. This observation further supports the late hemispherical resurfacing on this asteroid.

Acknowledgments and Data

The authors thank Dr. Lillian R. Ostrach and an anonymous reviewer for their extensive and insightful reviews of the manuscript. We thank the Hayabusa2 team for data acquisition and spacecraft operation. This study was supported by the JSPS Core-to-Core program "International Planetary Network", JSPS Grant-in-Aid KAKENHI (grant numbers JP19K14778, JP20H04607, JP20H00194, JP19H00727, JP17KK0097, JP17H06459, JP19H01951), the Astrobiology Center Program of National Institutes of Natural Sciences (NINS) (grant number AB311012), and the NASA Hayabusa2 Participating Scientist program (grant number NNX17AB36G to CME). M.H. acknowledges NASA/Solar System Workings (NNH17ZDA001N/80NSSC19K0548) and Auburn University/Intramural Grant Program. N.T. and K.Y. acknowledge funding support from International Graduate Program for Excellence in Earth-Space Science (IGPEES) from the University of Tokyo. All images are available at the JAXA Data Archives and Transmission System (DARTS) at www.darts.isas.jaxa.jp/.

References

Arakawa, M. et al. Artificial impact crater formed on the asteroid 162173 Ryugu in the gravity-dominated regime, *Science*, *368*(6486), 67-71, doi: 10.1126/science.aaz1701.

Bierhaus, E. B. et al. (2019), Asteroid (101955) Bennu's crater population: morphologies, size-frequency distribution, and consequences for surface age(s). *Lunar and Planetary Science Conference* 50, abstract 2496.

Bottke Jr., W. F., and R. Greenberg (1993), Asteroidal collision probabilities, *Geophys. Res. Lett.*, *20*(10), 879-881, doi:10.1029/92GL02713.

Bottke, W. F., M. C. Nolan, R. Greenberg, and R. A. Kolvoord (1994), Velocity Distributions among Colliding Asteroids, *Icarus*, *107*(2), 255-268, doi:10.1006/icar.1994.1021.

Bottke, W. F., D. D. Durda, D. Nesvorny, R. Jedicke, A. Morbidelli, D. Vokrouhlicky, and H. Levison (2005), The fossilized size distribution of the main asteroid belt, *Icarus*, *175*(1), 111-140, doi:10.1016/j.icarus.2004.10.026.

Bottke, W. F., D. Vokrouhlický, K. J. Walsh, M. Delbo, P. Michel, D. S. Lauretta, H. Campins, H. C. Connolly, D. J. Scheeres, and S. R. Chelsey (2015), In search of the source of asteroid (101955) Bennu: Applications of the stochastic YORP model, *Icarus*, *247*, 191-217, doi:10.1016/j.icarus.2014.09.046.

Chapman, C. R., W. J. Merline, P. C. Thomas, J. Joseph, A. F. Cheng, and N. Izenberg (2002), Impact History of Eros: Craters and Boulders, *Icarus*, *155*(1), 104-118, doi:10.1006/icar.2001.6744.

Cheng, A. F., N Izenberg, C. R. Chapman, and M. T. Zuber (2002), Ponded deposits on asteroid 433 Eros, *Meteorit. Planet. Sci.*, 37, 1095-1105. doi:10.1111/j.1945-5100.2002.tb00880.x.

Cloutis, E. A., et al. (2018), Spectral reflectance "deconstruction" of the Murchison CM2 carbonaceous chondrite and implications for spectroscopic investigations of dark asteroids, *Icarus*, *305*, 203-224, doi:10.1016/j.icarus.2018.01.015.

DellaGiustina, D. N. et al. (2020), Variations in color and reflectance on the surface of asteroid (101955) Bennu, *Science*, 370, eabc3660. doi: 10.1126/science.abc3660

1008 Flynn, G. J., and D. D. Durda (2004), Chemical and mineralogical size segregation in the impact
1009 disruption of inhomogeneous, anhydrous meteorites, *Planet. Space Sci.*, *52*(12), 1129-1140,
1010 doi:10.1016/j.pss.2004.07.010.
1011 Hirabayashi, M., D. P. Sánchez, and D. J. Scheeres (2015), Internal Structure of Asteroids Having
1012 Surface Shedding Due to Rotational Instability, *The Astrophysical Journal*, *808*(1), 63,
1013 doi:10.1088/0004-637x/808/1/63.
1014 Hirabayashi, M., et al. (2019), The Western Bulge of 162173 Ryugu Formed as a Result of a
1015 Rotationally Driven Deformation Process, *The Astrophysical Journal*, *874*(1), L10,
1016 doi:10.3847/2041-8213/ab0e8b.
1017 Hirata, N., et al. (2009), A survey of possible impact structures on 25143 Itokawa, *Icarus*, *200*(2), 486-
1018 502, doi:10.1016/j.icarus.2008.10.027.
1019 Hirata, N., et al. (2020), The spatial distribution of impact craters on Ryugu, *Icarus*, *338*,
1020 doi:10.1016/j.icarus.2019.113527.
1021 Housen, K. R., and K. A. Holsapple (2011), Ejecta from impact craters, *Icarus*, *211*(1), 856-875,
1022 doi:10.1016/j.icarus.2010.09.017.
1023 Kadono, T. et al. (2020), Impact experiment on asteroid (162173) Ryugu: Structure beneath the Impact
1024 point revealed by in situ observations of the ejecta curtain, *Astrophys. J. Lett.*, 899(1), L22,
1025 doi.org/10.3847/2041-8213/aba949
1026 Kanamaru, M. (2020), Dynamical evolution of small solar system bodies inferred from interior density
1027 distribution and YORP-induced spin alteration, (Doctoral dissertation). Osaka, Japan: Osaka
1028 University.
1029 Keil, K., D. Stöffler, S. G. Love, and E. R. D. Scott (1997), Constraints on the role of impact heating
1030 and melting in asteroids, *Meteorit. Planet. Sci.*, *32*(3), 349-363, doi:10.1111/j.1945-
1031 5100.1997.tb01278.x.
1032 Kikuchi, H., et al. (2019), 3D mapping of structural features on Ryugu, *Lunar and Planetary Science*
1033 *Conference* 50, abstract 2409.
1034 Kikuchi, S., et al. (2020), Hayabusa2 Landing Site Selection: Surface Topography of Ryugu and
1035 Touchdown Safety, *Space Sci. Rev.* 216, 116, doi.org/10.1007/s11214-020-00737-z.
1036 Kitazato, K., et al. (2019), The surface composition of asteroid 162173 Ryugu from Hayabusa2 near-
1037 infrared spectroscopy, *Science*, *364*(6437), 272-275, doi:10.1126/science.aav7432.
1038 Matsumoto, K., et al. (2020), Improving Hayabusa2 trajectory by combining LIDAR data and a shape
1039 model, *Icarus*, *338*, doi:10.1016/j.icarus.2019.113574.
1040 Maxwell, D. E. (1977) *Impact and Explosion Cratering: Planetary and Terrestrial Implications*, D. J.
1041 Roddy, R. O. Pepin, R. B. Merrill, Eds. (Pergamon Press, 1977), pp. 1003–1008.
1042 Melosh, H. J. (1989), *Impact Cratering -A Geologic Process-*, Oxford University Press, New York.
1043 Michel, P., and M. Delbo (2010), Orbital and thermal evolutions of four potential targets for a sample
1044 return space mission to a primitive near-Earth asteroid, *Icarus*, *209*(2), 520-534,
1045 doi:10.1016/j.icarus.2010.05.013.
1046 Michel, P., et al. (2020), Collisional formation of top-shaped asteroids and implications for the origins
1047 of Ryugu and Bennu, *Nat Commun*, *11*(1), 2655, doi:10.1038/s41467-020-16433-z.
1048 Michikami, T., et al. (2019), Boulder size and shape distributions on asteroid Ryugu, *Icarus*, *331*, 179-
1049 191, doi:10.1016/j.icarus.2019.05.019.
1050 Miyamoto, H., et al. (2007), Regolith migration and sorting on asteroid Itokawa, *Science*, *316*(5827),
1051 1011-1014, doi:10.1126/science.1134390.
1052 Morota, T., et al. (2020), Sample collection from asteroid (162173) Ryugu by Hayabusa2: Implications
1053 for surface evolution, *Science*, *368*, 654-659, doi:10.1126/science.aaz6306.
1054 Nagao, K., et al. (2011), Irradiation history of Itokawa regolith material deduced from noble gases in
1055 the Hayabusa samples, *Science*, *333*(6046), 1128-1131, doi:10.1126/science.1207785.
1056 Namiki, N., et al. (2019), Topography of large craters of 162173 Ryugu. *Lunar and Planetary Science*
1057 *Conference* 50, abstract 2658.
1058 Nishiyama, G., Kawamura, T., Namiki, N., Fernando, B., Leng, K., Onodera, K., et al.
1059 (2020). Simulation of seismic wave propagation on asteroid ryugu induced by the impact
1060 experiment of the hayabusa2 mission: limited mass transport by low yield strength of porous
1061 regolith. *Journal of Geophysical Research: Planets*, 121,
1062 e2020JE006594. https://doi.org/10.1029/2020JE006594

1063 Noguchi, R. et al. (2021), Crater depth-to-diameter ratios on asteroid 162173 Ryugu, Icarus, 354,
1064 114016, doi.org/10.1016/j.icarus.2020.114016.
1065 Nolan, M. C., E. S. Howell, D. J. Scheeres, J. W. McMahon, O. Golubov, C. W. Hergenrother, J. P.
1066 Emery, K. S. Noll, S. R. Chesley, and D. S. Lauretta (2019), Detection of Rotational Acceleration
1067 of Bennu Using HST Light Curve Observations, *Geophys. Res. Lett.*, *46*(4), 1956-1962,
1068 doi:10.1029/2018gl080658.
1069 Oberbeck, V. R. (1971), Laboratory simulation of impact cratering with high explosives, *Journal of*
1070 *Geophysical Research*, *76*(23), 5732-5749, doi:10.1029/JB076i023p05732.
1071 O'Brien, D. P., and R. Greenberg (2005), The collisional and dynamical evolution of the main-belt and
1072 NEA size distributions, *Icarus*, *178*(1), 179-212, doi:10.1016/j.icarus.2005.04.001.
1073 Robinson, M. S., P. C. Thomas, J. Veverka, S. Murchie, and B. T. Carcich. (2001), The nature of ponded
1074 deposits on Eros, *Nature*, 413, 396-400.
1075 Scheeres, D. J., et al. (2020), Particle Ejection Contributions to the Rotational Acceleration and Orbit
1076 Evolution of Asteroid (101955) Bennu, *J. Geophys. Res. Planets*, *125*(3),
1077 doi:10.1029/2019je006284.
1078 Statler, T. S. (2009), Extreme sensitivity of the YORP effect to small-scale topography, *Icarus*, *202*(2),
1079 502-513, doi:10.1016/j.icarus.2009.03.003.
1080 Sugita, S., et al. (2019), The geomorphology, color, and thermal properties of Ryugu: Implications for
1081 parent-body processes, *Science*, *364*(6437), 252, doi:10.1126/science.aaw0422.
1082 Suzuki, H., et al. (2018), Initial inflight calibration for Hayabusa2 optical navigation camera (ONC) for
1083 science observations of asteroid Ryugu, *Icarus*, *300*, 341-359, doi:10.1016/j.icarus.2017.09.011.
1084 Tatsumi, E., and S. Sugita (2018), Cratering efficiency on coarse-grain targets: Implications for the
1085 dynamical evolution of asteroid 25143 Itokawa, *Icarus*, *300*, 227-248,
1086 doi:10.1016/j.icarus.2017.09.004.
1087 Tatsumi, E., et al. (2019), Updated inflight calibration of Hayabusa2's optical navigation camera (ONC)
1088 for scientific observations during the cruise phase, *Icarus*, *325*, 153-195,
1089 doi:10.1016/j.icarus.2019.01.015.
1090 Veverka, J., et al. (1999), NEAR Encounter with Asteroid 253 Mathilde: Overview, *Icarus*, *140*(1), 3-
1091 16, doi:10.1006/icar.1999.6120.
1092 Veverka, J., et al. (2001) Imagin of small-scale features on 433 Eros from NEAR: Evidence for a
1093 complex regolith, *Science*, 292, 484-488.
1094 Walsh, K. J., et al. (2019), Craters, boulders and regolith of (101955) Bennu indicative of an old and
1095 dynamic surface, *Nature Geosci.*, *12*, 242-246, doi:10.1038/s41561-019-0326-6.
1096 Watanabe, S., et al. (2019), Hayabusa2 arrives at the carbonaceous asteroid 162173 Ryugu-A spinning
1097 top-shaped rubble pile, *Science*, *364*(6437), 268-272, doi:10.1126/science.aav8032.
1098 Wünnemann, K., G. S. Collins, and H. J. Melosh (2006), A strain-based porosity model for use in
1099 hydrocode simulations of impacts and implications for transient crater growth in porous targets,
1100 *Icarus*, *180*(2), 514-527, doi:10.1016/j.icarus.2005.10.013.
1101 Yamada, T. M., K. Ando, T. Morota, and H. Katsuragi (2016), Timescale of asteroid resurfacing by
1102 regolith convection resulting from the impact-induced global seismic shaking, *Icarus*, *272*, 165-
1103 177, doi:10.1016/j.icarus.2016.02.032.
1104 Yokota, Y. et al. Opposition observations of 162173 Ryugu: Normal albedo map highlights variations
1105 in regolith characteristics, *Planetary Science Journal*, in revision